

Compositional Variations in Sedimentary Deposits in Gale Crater as Observed by ChemCam Passive and Active Spectra

Henry Manelski¹, Rachel Y. Sheppard², Abigail A. Fraeman³, Roger C. Wiens⁴, Jeffrey R. Johnson⁵, Elizabeth B. Rampe⁶, Jens Frydenvang⁷, Nina L. Lanza⁴, and Olivier Gasnault⁸

¹Purdue University

²Planetary Science Institute

³Jet Propulsion Laboratory, California Institute of Technology

⁴Los Alamos National Laboratory (DOE)

⁵Johns Hopkins University Applied Physics Laboratory

⁶NASA Johnson Space Center

⁷University of Copenhagen

⁸Institut de Recherche en Astrophysique et Planétologie (IRAP)

January 3, 2023

Abstract

During the first 2934 sols of the Curiosity rover's mission 33,468 passive visible/near-infrared reflectance spectra were taken of the surface by the mast-mounted ChemCam instrument on a range of target types. ChemCam spectra of bedrock targets from the Murray and Carolyn Shoemaker formations on Mt. Sharp were investigated using principal component analysis (PCA) and various spectral parameters including the band depth at 535 nm and the slope between 840 nm and 750 nm. Four endmember spectra were identified. Passive spectra were compared to Laser Induced Breakdown Spectroscopy (LIBS) data to search for correlations between spectral properties and elemental abundances. The correlation coefficient between FeOT reported by LIBS and BD535 from passive spectra was used to search for regions where iron may have been added to the bedrock through oxidation of ferrous-bearing fluids, but no correlations were found. Rocks in the Blunts Point-Sutton Island transition that have unique spectral properties compared to surrounding rocks, that is flat near-infrared (NIR) slopes and weak 535 nm absorptions, are associated with higher Mn and Mg in the LIBS spectra of bedrock. Additionally, calcium-sulfate cements, previously identified by Ca and S enrichments in the LIBS spectra of bedrock, were also shown to be associated with spectral trends seen in Blunts Point. A shift towards steeper near-infrared slope is seen in the Hutton interval, indicative of changing depositional conditions or increased diagenesis.

Hosted file

951685_0_art_file_10516196_rmj5zs.docx available at <https://authorea.com/users/564999/articles/612020-compositional-variations-in-sedimentary-deposits-in-gale-crater-as-observed-by-chemcam-passive-and-active-spectra>

55 **Abstract**

56 During the first 2934 sols of the Curiosity rover's mission 33,468 passive visible/near-infrared
57 reflectance spectra were taken of the surface by the mast-mounted ChemCam instrument on a
58 range of target types. ChemCam spectra of bedrock targets from the Murray and Carolyn
59 Shoemaker formations on Mt. Sharp were investigated using principal component analysis
60 (PCA) and various spectral parameters including the band depth at 535 nm and the slope
61 between 840 nm and 750 nm. Four endmember spectra were identified. Passive spectra were
62 compared to Laser Induced Breakdown Spectroscopy (LIBS) data to search for correlations
63 between spectral properties and elemental abundances. The correlation coefficient between FeO_T
64 reported by LIBS and BD535 from passive spectra was used to search for regions where iron
65 may have been added to the bedrock through oxidation of ferrous-bearing fluids, but no
66 correlations were found. Rocks in the Blunts Point-Sutton Island transition that have unique
67 spectral properties compared to surrounding rocks, that is flat near-infrared (NIR) slopes and
68 weak 535 nm absorptions, are associated with higher Mn and Mg in the LIBS spectra of bedrock.
69 Additionally, calcium-sulfate cements, previously identified by Ca and S enrichments in the
70 LIBS spectra of bedrock, were also shown to be associated with spectral trends seen in Blunts
71 Point. A shift towards steeper near-infrared slope is seen in the Hutton interval, indicative of
72 changing depositional conditions or increased diagenesis.

73

74 **Plain Language Summary**

75 The Chemistry and Camera (ChemCam) instrument on the Mars Science Laboratory Curiosity
76 rover was built for use in 'active' mode: in which a laser vaporizes a small amount of material
77 from a targets' surface and the light emitted from the resulting plasma is used to quantify the
78 relative amounts of various elements. ChemCam also collects 'passive' spectra (without the use
79 of the laser). These passive spectra use reflected sunlight to provide complementary
80 mineralogical information. By looking at how passive and active spectral features relate and
81 change we can further our understanding of the composition of targets that the rover has
82 encountered. Comparison between passive spectral parameters and iron oxides reported by active
83 spectroscopy identified two regions (Sutton Island to Blunts Point and Glasgow to Knockfarril
84 Hill transitions) as areas of compositional interest and show evidence of variations in oxidation
85 conditions. The passive spectra are also shown to be largely in agreement with data from
86 CheMin, another instrument on Curiosity which provides mineralogical analysis of powdered
87 samples.

88

89 **1. Introduction**

90 The Mars Science Laboratory's (MSL) Curiosity rover landed on the northern plains of Gale
91 crater, a ~154 km diameter impact crater in southern Elysium Planitia, along the planetary
92 dichotomy, in August of 2012. Since landing, Curiosity has travelled across the crater floor and
93 then up the side of Mt. Sharp (formally known as Aeolis Mons) with a goal to characterize the
94 past environments preserved in the region's sedimentary rock record, and to determine if these
95 environments would have been habitable (Vasavada, 2022 and references therein).

96

97 Visible and near-infrared (VNIR, ~400-1000 nm) reflectance spectroscopy plays a key role in the
98 suite of tools Curiosity uses to identify the composition of materials it encounters. This spectral
99 range is sensitive to broad charge-transfer and crystal field absorptions that are most commonly
100 associated with iron-bearing minerals (e.g. Wellington et al., 2017). Curiosity's Mast Camera

101 (Mastcam) measures relative reflectance of the surface from 400-1020 nm in up to 12 unique
102 wavelengths (Bell et al., 2017; Malin et al., 2017). Multispectral observations have been
103 demonstrated to discriminate compositionally distinct materials in Gale Crater, and they
104 qualitatively agree with mineralogy from samples measured by Curiosity's X-ray diffraction
105 instrument (Horgan et al., 2020; Jacob et al., 2020; Wellington et al., 2017). Large scale surveys
106 of the VNIR spectral properties of rocks, soils, and veins along Curiosity's traverse conducted
107 using Mastcam data from sols 0-2302 have been interpreted to reveal nine rock spectral classes
108 (Rice et al., 2022). The spectral differences between classes were understood to be caused
109 predominantly by variations in grain size and abundance of hematite and other iron oxides (Rice
110 et al., 2022). Rock spectral variability was also observed to align with stratigraphic members in
111 some cases (Horgan et al., 2020; Rice et al., 2022).

112
113 Early in Curiosity's mission, a novel protocol was developed to calibrate passive radiance
114 measurements from the Chemistry and Camera (ChemCam) (i.e., without the use of ChemCam's
115 laser) to relative reflectance using well-characterized Mastcam and ChemCam calibration
116 targets, creating a VNIR relative reflectance spectra dataset (Johnson, 2022; Johnson et al.,
117 2015). In contrast to Mastcam, which is an imager, ChemCam collects point spectra from spots
118 that are nanometers to micrometers in size. Like Mastcam spectra, ChemCam relative reflectance
119 spectra proved useful in classifying material near Curiosity's landing site and observing airfall
120 dust coverage and have been shown to be sensitive to mineralogy, with the ability to distinguish
121 major Fe-bearing minerals (e.g., hematite and ferric sulfates) in Mt. Sharp, sometimes as far
122 away as several kilometers (Johnson et al., 2015, 2016). ChemCam passive spectra have also
123 been demonstrated to be consistent with Chemistry and Mineralogy (CheMin) X-ray diffraction
124 data (Johnson et al., 2016; Wellington et al., 2017).

125
126 In active mode, ChemCam uses laser ablation in the form of laser induced breakdown
127 spectroscopy (LIBS) to investigate rocks and regolith in Gale Crater (Maurice et al., 2012; Wiens
128 et al., 2012). LIBS provides information about the elemental composition of geologic materials
129 and is especially valuable because it can be used to investigate targets several meters away,
130 removes most of the airfall dust from the observation area (Graff et al., 2011; Johnson et al.,
131 2015), and has the ability to sense chemical changes with depth (Lanza et al., 2012). ChemCam
132 acquires a passive spectrum before and/or after each LIBS observation, so almost all the passive
133 reflectance spectra pair one-to-one with a LIBS elemental abundance measurement. The
134 correlated LIBS elemental chemistry and passive spectral datasets therefore provide a unique
135 resource to track how the reflectance properties and chemical composition varied over the course
136 of the traverse at the nanometer to micrometer scale.

137
138 This paper expands upon and complements previous investigations of ChemCam passive and
139 Mastcam spectral data of rocks in the lower portion of Mt. Sharp (Fraeman et al., 2020; Haber et
140 al., 2022; Horgan et al., 2020; Jacob et al., 2020; Johnson et al., 2015, 2016; Rice et al., 2022;
141 Wellington et al., 2017). Here, the spectral properties of bedrock targets in Mt. Sharp's Murray
142 and Carolyn Shoemaker formations observed by ChemCam passive spectra are studied using
143 principal component analysis (PCA) along with band depth and spectral slope/ratio calculations.
144 This spectral dataset comprises a subset of 9,400 passive spectra acquired between sols 776 and
145 2934 of Curiosity's mission. This work also for the first time investigates paired ChemCam
146 LIBS elemental composition data and passive reflectance spectra with the goal to investigate the

147 source(s) and implications of spectral trends seen in the ChemCam passive data set. Where
148 available, ChemCam data are also compared with mineralogy reported by the Chemistry and
149 Mineralogy (CheMin) instrument to search for further insight into sources of spectral variability.
150

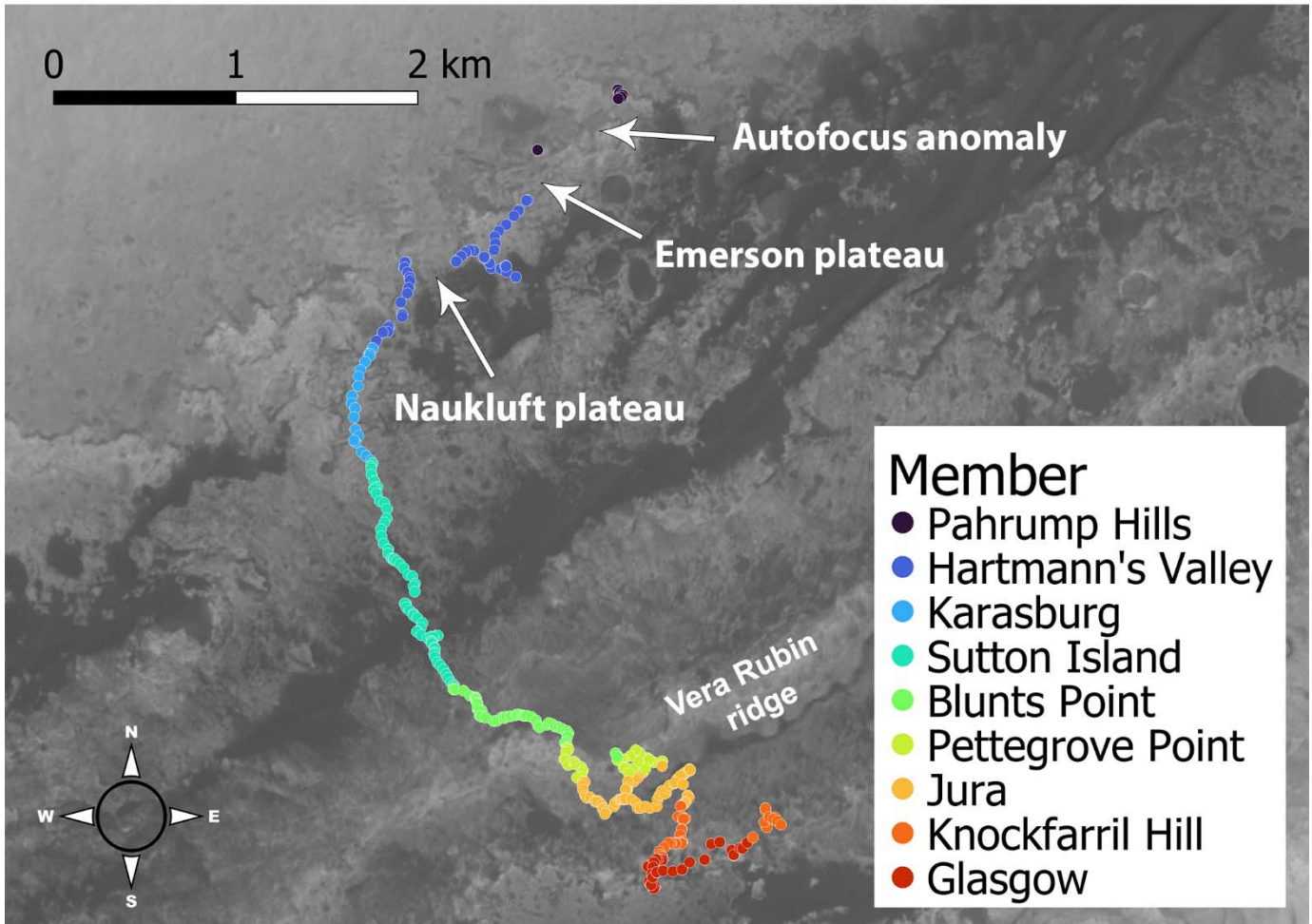
151 **2. Background**

152 **2.1 Mount Sharp Geology**

153 Gale crater is a ~3.7-billion-year-old impact feature near the boundary of the northern highlands
154 and southern lowlands of Mars (e.g., Pelkey & Jakosky, 2002). Gale crater contains a central
155 mound, Mount Sharp, that rises ~5.5 km above the surrounding terrain (e.g., Thomson et al.,
156 2011) and provides an unprecedented opportunity to examine hundreds of meters of stratigraphy
157 that may preserve clues to the past climate history and habitability of Mars.
158

159 The sedimentary rocks that Curiosity has traversed can be divided into three geologic groups: (1)
160 the Bradbury group, where Curiosity landed and explored for the first 776 sols of its mission, is
161 composed of diverse sedimentary units including fluvial, aeolian, and lacustrine deposits along
162 the crater floor; (2) the Mount Sharp group, which is the sedimentary group that makes up the
163 primary structure of Mount Sharp; and (3) the Siccar Point group, which unconformably overlies
164 the Mount Sharp group and is composed of younger aeolian sandstone deposits (Vasavada,
165 2022). This paper will focus on the Mount Sharp group prior to sol 2934.
166

167 The Mount Sharp group has been subdivided into several formations and members by the MSL
168 Team (Fig. 1; Table 1). The Murray formation is ~300 m thick and is composed of the Pahrump
169 Hills, Hartmann's Valley, Karasburg, Sutton Island, Blunts Point, Pettegrove Point, and Jura
170 stratigraphic members. This formation was predominantly deposited in lacustrine and marginal
171 lacustrine environments (Edgar et al., 2020; Gwizd et al., 2022; Stack et al., 2019). The ~70 m
172 thick Carolyn Shoemaker formation sits above the Murray formation, and it subdivides into the
173 Knockfarril Hill and Glasgow members. The Carolyn Shoemaker formation has an increased
174 diversity of depositional environments compared to the Murray formation, including evidence
175 for higher energy fluvial systems (Bennett et al., 2022; Caravaca et al., 2022; Vasavada, 2022,
176 Fedo et al., 2022).



177 **Figure 1.** All ChemCam bedrock targets in the Murray and Carolyn Shoemaker formations, up
 178 to sol 2934, colored by stratigraphic member (Table 1). Gaps in the earlier part of the data are
 179 due to traversing aeolian strata at Emerson and Naukluft Plateaus, and to a temporary anomaly
 180 with ChemCam's autofocus. Knockfarril Hill and Glasgow are part of the Carolyn Shoemaker
 181 formation, all other members are part of the Murray Formation. The base map is a CTX 6 meter
 182 mosaic (Calef & Parker, 2016).

183
 184
 185

Table 1. Stratigraphic Members in the Mt. Sharp group

Stratigraphic formation	Stratigraphic member	Approximate sol range	Elevation relative to MOLA datum (m)
Murray	Pahrump Hills	776-797, 807-950, 997-1035, 1067-1072	-4460 to -4437
Murray	Hartmann's Valley	1105-1108, 1154-1276, 1354-1412	-4437 to -4412
Murray	Karasburg	1413-1473	-4412 to -4375

Murray	Sutton Island	1474-1690	-4375 to -4280
Murray	Blunts Point	1691-1809, 2046-2094	-4280 to -4210
Murray	Pettegrove Point	1810-1873, 2000-2014, 2024-2045, 2095-2157,	-4210 to -4172
Murray	Jura	1874-1999, 2015-2023, 2158-2439, 2448-2453	-4172 to -4143
Carolyn Shoemaker	Knockfarril Hill	2440-2447, 2454-2606, 2817-2950	-4143 to -4117
Carolyn Shoemaker	Glasgow	2607-2695, 2735-2816	-4117 to 4072

186 **Note.** Geological member/formation sol (Martian day) ranges and elevations (Edgar et al., 2020;
187 Fedo et al., 2022; Gwizd et al., 2022; Stack et al., 2016)

188

189 2.2 Spectral Features

190 The wavelength range of ChemCam’s passive spectral measurements is sensitive to electronic
191 transitions, including charge transfer and crystal field splitting. Crystalline ferric oxides and
192 oxyhydroxides including crystalline hematite have four characteristic broad electronic
193 absorptions in this range: 400-415 nm, 485-550 nm, 650-710 nm, and 804-910 nm (Morris et al.,
194 1985; Sherman et al., 1982; Sherman, 1985; Sherman & Waite, 1985). Poorly crystalline,
195 nanophase Fe oxides lack these distinct spectral absorptions and are characterized by a steep
196 spectral edge between 400-750 nm (Bell et al., 1990, 2000). Magnetite, a mixed-valence Fe
197 oxide, has a relatively flat, low-reflectance spectrum with a local minimum near 550 nm and
198 local maximum near 650 nm, caused by closely co-located Fe²⁺ and Fe³⁺ in both tetrahedral and
199 octahedral coordination (Izawa et al., 2019). Although a variety of factors (e.g., particle size,
200 opaque minerals) can influence the strength of an absorption band in reflectance spectra,
201 calculating relevant band depth, band positions, and spectral slopes can provide a measurement
202 of relative absorption strength between samples.

203

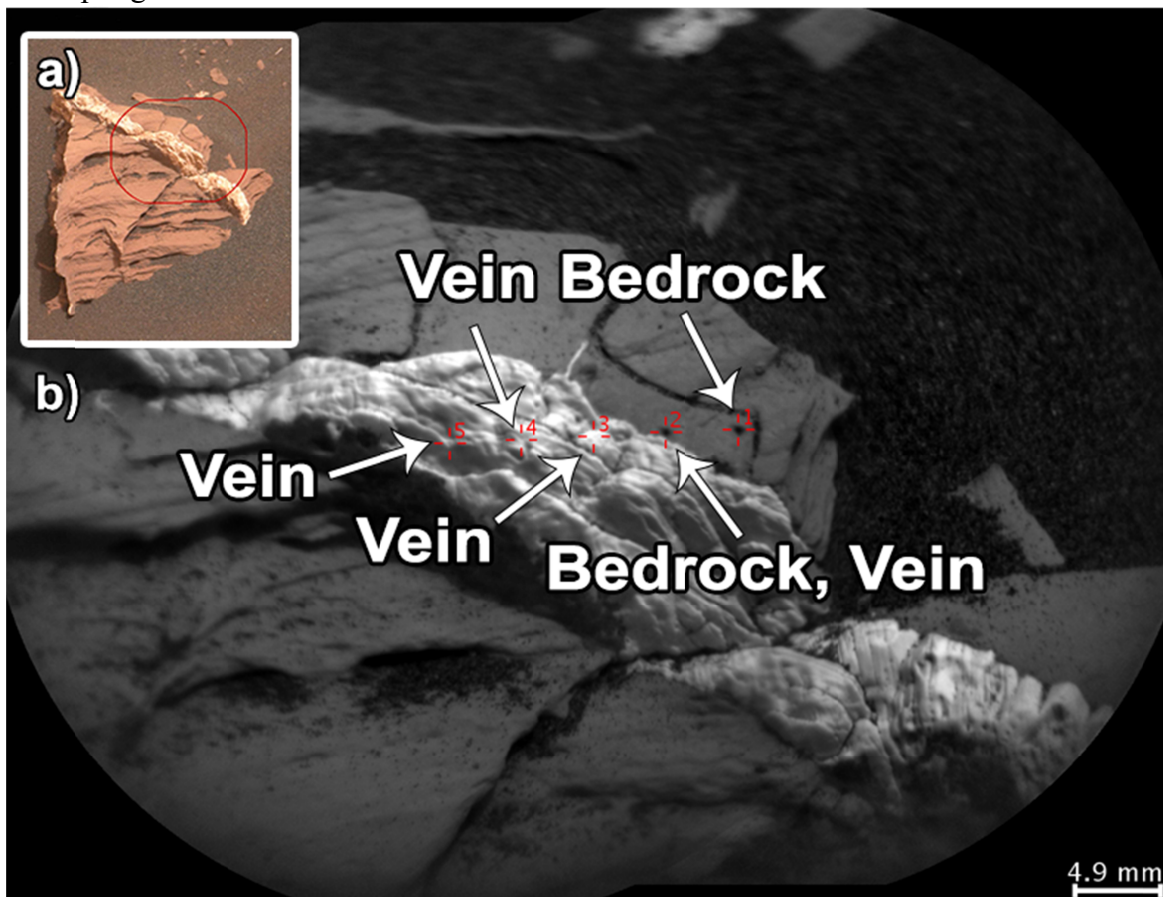
204 3. Methods

205 3.1 ChemCam Passive Spectral Data Acquisition and Treatment

206 ChemCam passive surface spectral data calibrated to relative reflectance using the methods
207 described in Johnson et al., (2015, 2016) are available from NASA’s Planetary Data System
208 (PDS) Geosciences Node (Johnson, 2022). ChemCam uses three spectrometers to measure
209 reflected radiance: the UV spectrometer (240.1-342.2 nm), violet (VIO) spectrometer (382.1-
210 469.4 nm), and visible/near infrared (VNIR) spectrometer (474.0-906.5 nm) (Wiens et al., 2012).
211 Passive spectra are restricted to 440-840 nm because the UV spectrometer responsivity, VIO
212 spectrometer responsivity <440 nm, and VNIR spectrometer responsivity >840 nm are relatively
213 low, resulting in low SNR in the passive reflectance spectra (Johnson et al., 2015). Data near the
214 detector edges around the gap between the VIO and VNIR spectrometers, from ~469-474 nm,
215 are also associated with low SNR due to low detector responsivity (Wiens et al., 2012). The
216 trimmed spectra were passed through a Savitzky-Golay filter (SG) for smoothing, which fit
217 subsets of nearby points with a cubic polynomial via linear least squares (Savitzky & Golay,

218 1964). This smoothing step ensured that spectral features were not a result of localized noise.
219 Spectra that had at least one negative value for relative reflectance between 440-840 nm after
220 filtering (256 spectra) were deemed invalid and removed from the dataset. Spectra were co-
221 registered with orbital basemaps using QGIS, and MSL localizations from the sol the spectra
222 were acquired were used to assign each measurement a latitude and longitude (Deen, 2015).
223

224 ChemCam surface reflectance passive spectra of each observation were manually classified by
225 Johnson (2022) into target types such as bedrock, veins, calibration targets, soils, and sands. An
226 example of 1x5 ChemCam raster target that covers vein, bedrock, and mixed vein and bedrock
227 classified material is shown in Fig. 2. Of the 33,631 passive spectra taken in the first 2934 sols,
228 16,246 (48.3%) are solely categorized as bedrock targets. Only Murray and Carolyn Shoemaker
229 formation targets classified as “bedrock” collected prior to sol 2934 were included in the
230 analyses described below (9,400 observations). It is important to note LIBS measurements give
231 information about a smaller radius of material due to the narrower size of the laser beam
232 compared to the spectrometer IFOV (~400 μm for the laser spot size vs. ~1.3-2.6 mm for the
233 ChemCam passive spectral for targets 2-4 m away; Maurice et al., 2012; Wiens et al., 2012), so
234 their sampling areas are different.



235 **Figure 2.** Example of different types of ChemCam target materials (target Tofte on sol 2080). (a)
236 The red ellipse in this Mastcam mosaic context image shows the location of the RMI. (b) Each of
237 the red crosshairs in this RMI image corresponds to a LIBS and passive spectral target. Target
238 type classifications for each point are shown.
239

240 **3.2 Spectral characterization**

241 The shape and location of a spectral absorption, as well as the overall shape of the spectrum
 242 itself, can be described by numerical parameterizations such as band depths and spectral slopes.
 243 Previous studies have found several spectral parameters that are particularly effective for
 244 evaluating characteristics of ChemCam passive spectra, summarized in Table 2 (Johnson et al.,
 245 2015, 2016).

246
 247 **Table 2.** Equations to Calculate Spectral Parameters (Fraeman et al., 2020; Johnson et al., 2015).
 248

Spectral parameter	Equation	Description
BD535	$1 - \frac{R_{535}^*}{0.65R_{500}^* + 0.35R_{600}^*}$	Positive when Fe ³⁺ is present
BD600	$1 - \frac{R_{600}^*}{0.52R_{535}^* + 0.48R_{670}^*}$	Related to the strength of the short wavelength ferric oxide absorption edge
R6744	$\frac{R_{670}^*}{R_{440}^*}$	VIS ratio, related to airfall dust coverage
R6084	$\frac{R_{840}^*}{R_{600}^*}$	NIR ratio
S7584	$\frac{R_{840}^* - R_{750}^*}{(840 - 750)}$	NIR slope, indicative of the strength of iron absorptions
Spectral Maximum	NA	Wavelength at which R* is highest.
Average relative reflectance	$\frac{\sum R^*}{2462}$	Average relative reflectance of a target from 440 to 840 nm

249 **Note.** R_{###}* is the relative reflectance after smoothing with the Savitsky-Golay filter at ### nm.
 250 Average relative reflectance is the sum of the relative reflectance divided by the total number of
 251 channels between 440 and 840 nm (2462).
 252

253 Two prominent spectral parameters used here were the band depth at 535 nm (BD535) and slope
 254 between 840 nm and 750 nm (S7584) (Table 2). The absorption at 535 nm is caused by the
 255 presence of ferric phases. The slope from 840-750 nm can be a proxy for a broad absorption
 256 feature centered at ~860 nm, which is related to some ferric phases such as hematite (Morris et
 257 al., 1985), although it can also be sensitive to the broad Fe²⁺ absorption near 1000 nm associated
 258 with olivine and pyroxene. Combined, large BD535 and S7584 values have been confirmed to

259 provide evidence for the presence of ferric phases (Fraeman et al., 2020; Jacob et al., 2020;
260 Wellington et al., 2017).

261

262 **3.3 LIBS Elemental Abundance Data**

263 ChemCam LIBS spectra were converted into major oxide compositions (MOC) via a calibration
264 model that uses a weighted average of two multivariate approaches: partial least squares and
265 independent component analysis (Clegg et al., 2017). This model was trained on a diverse set of
266 408 pressed power samples with independently measured compositions and cross validation was
267 used to tune relevant modelling parameters. The result is MOC tables that report wt% of various
268 oxides as well as corresponding Root Mean Squared Error of Prediction (RMSEP) values for all
269 points analyzed by LIBS. These MOC tables are available from the PDS Geosciences Node
270 (Wiens, 2022).

271

272 ChemCam acquires a passive spectrum before or after each LIBS observation, so almost all the
273 passive spectra of bedrock in the Murray and Carolyn Shoemaker formations pair one-to-one
274 with a LIBS elemental abundance measurement. The correlated LIBS elemental chemistry and
275 passive spectral datasets allow for tracking how the spectral properties compare with chemical
276 composition, and how both changed over the course of the traverse. Although data were acquired
277 between sols 801 and 985, during the resolution of the ChemCam autofocus problem (Peret et
278 al., 2016), the mode of observation during this period makes it more difficult to match LIBS and
279 passive spectra, so this period was not considered in this study (Fig. 1). There is also a subset of
280 “passive only” targets, where data were collected without LIBS (Johnson et al., 2015, 2016), and
281 those targets are also not included in this work. All major oxides reported by ChemCam (FeO_T ,
282 MgO , SiO_2 , CaO , Na_2O , K_2O , TiO_2 , and Al_2O_3) were included in the analysis, as was MnO
283 (Gasda et al., 2021). Iron abundances are given as FeO , regardless of the actual oxidation state,
284 because the oxidation state is not determined by routine LIBS analysis.

285

286 **3.4 Principal Component Analysis (PCA)**

287 PCA is a dimensionality reduction technique which converts a n-dimensional data cloud into
288 orthogonal principal components (PCs) sorted from high to low percentages of the variance in
289 the dataset that can be summarized with only a few axes, to aid in analysis (Pearson, 1901). PCA
290 was conducted on the passive spectral data from ChemCam using the scikit-learn library in
291 Python (Pedregosa et al., 2012). To understand the influence of compositional features on the
292 dataset and subsequent major PCs, the PCs were plotted against each other, spectral parameters
293 (as described in Section 3.2), and LIBS elemental abundances. Correlations were reported using
294 Spearman’s rank correlation coefficient, which describes how well the relationship between two
295 variables can be expressed a monotonic function (Spearman, 1904). PCA has proved useful in
296 capturing the variability of ChemCam LIBS spectra (Anderson et al., 2011) and also has been
297 applied to analyses of planetary reflectance spectral datasets (Farrand et al., 2013). Loading plots
298 show the wavelength contributions to each PC and were very helpful in interpreting the meaning
299 of PC values. Positive loadings for a PC in a given wavelength region mean that higher
300 reflectance in that range would lead to higher values for that PC; negative loadings for a PC in a
301 given wavelength region mean that higher reflectance in that range would lead to lower values
302 for that PC. The terms “contribute positively” and “contribute negatively” (to a given PC) are
303 used to describe positive and negative loadings. The distance from zero indicates the relative
304 influence at a given wavelength.

305 **3.5 CheMin Data**

306 The CheMin instrument uses X-ray diffraction to measure the presence and abundance of
307 minerals and X-ray amorphous materials in drilled rock and scooped soil samples in Gale crater
308 (Blake et al., 2012). CheMin observations were compared to ChemCam passive spectral
309 parameters to see how ferric minerals affect the relative reflectance data. CheMin requires
310 sample processing (i.e., drilling or scooping), and as a result there are far fewer observations
311 compared to ChemCam. CheMin typically analyzes a sample drilled from a depth of 3-4 cm
312 (Anderson et al., 2012), whereas ChemCam only probes a few micrometers below the surface
313 per laser shot (Maurice et al., 2012). Analyses of CheMin data identify ~20-70% X-ray
314 amorphous materials in every sample measured to date, and it is very difficult to characterize the
315 identity of the amorphous material(s) from the XRD data alone (Rampe et al., 2020a). The
316 amorphous component may have a substantial impact on the target's reflectance data because
317 mass balance calculations of the amorphous component composition using CheMin and APXS
318 data suggest the amorphous component is typically enriched in FeO_T, potentially corresponding
319 to nanophase ferric oxides (e.g., Rampe et al., 2020a).

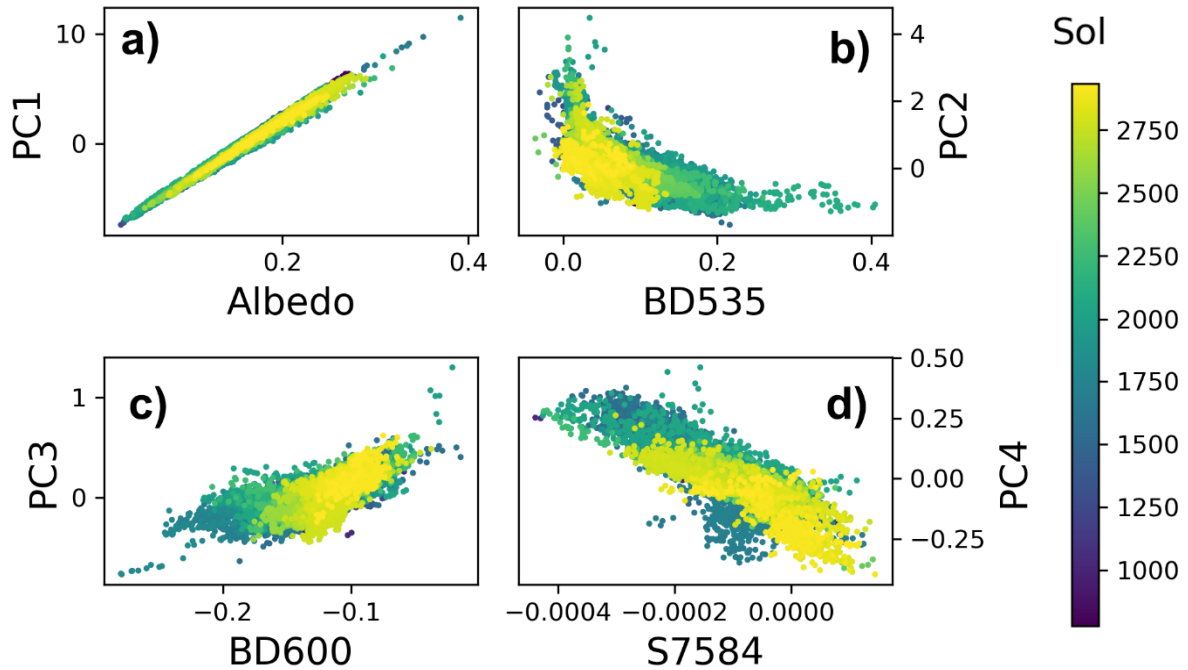
320

321 **4. Results**

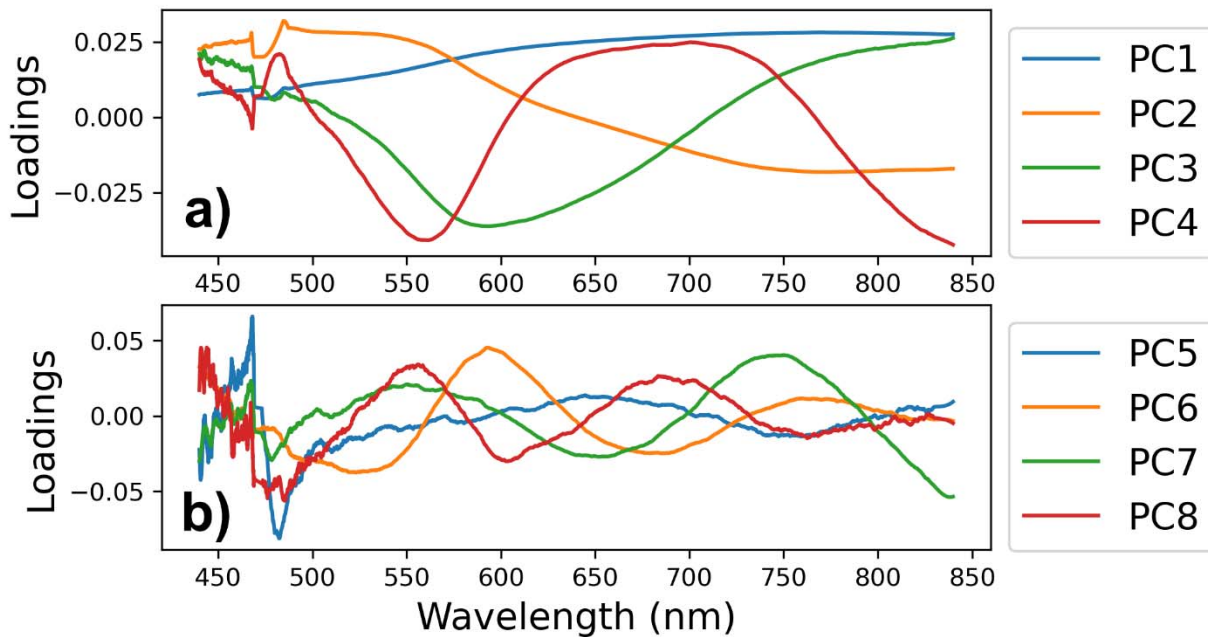
322 **4.1 Principal Component Analysis**

323 The first principal component (PC1) accounted for 92.62% of the variance in the dataset and was
324 strongly correlated with average relative reflectance (Spearman's $\rho = 0.99$; Fig. 3a). PC1's
325 loadings were all positive and mirrored the average ChemCam reflectance spectrum, as expected
326 (Fig. 4a). PC2 explained 6.61% of the variance and was negatively correlated with BD535 (Fig.
327 3b) and R6744 and positively correlated with R6084 ($\rho = -0.73, -0.90, \text{ and } 0.80$ respectively).
328 The wavelength range around 535 nm contributed positively to PC2 and wavelengths between
329 750 and 840 nm contributed negatively (Fig. 4a). PC3 was weakly correlated with BD600 (Fig.
330 3c, $\rho = 0.60$). Wavelengths 550 nm to 650 nm contributed negatively and 750 nm to 840 nm
331 wavelengths contributed positively to PC3 (Fig. 4a). PC4 was negatively correlated with S7584
332 (Fig. 3d) and the spectral maximum ($\rho = -0.85$ and -0.72 respectively). The areas around 560 nm
333 and past 800 nm contributed negatively to PC4, whereas the 600 nm to 725 nm region
334 contributed positively (Fig. 4a). PC3 and PC4 explained 0.42% and 0.23% of the variance
335 respectively. The loading plots for PC5 through PC8 show a significant increase in volatility
336 below 500 nm and an increase in noise overall (Fig. 4b). Cumulatively explaining less than
337 0.12% of the variance of the passive spectral dataset, PCs past PC4 were not found to
338 meaningfully relate to any spectral features in the dataset. Fig. 5 shows PC2 plotted against PC1
339 and PC4 plotted against PC3 – as expected the PCs are not correlated with one another. Fig. 6
340 shows representative ChemCam spectra for maximum and minimum values for PCs 1-4.

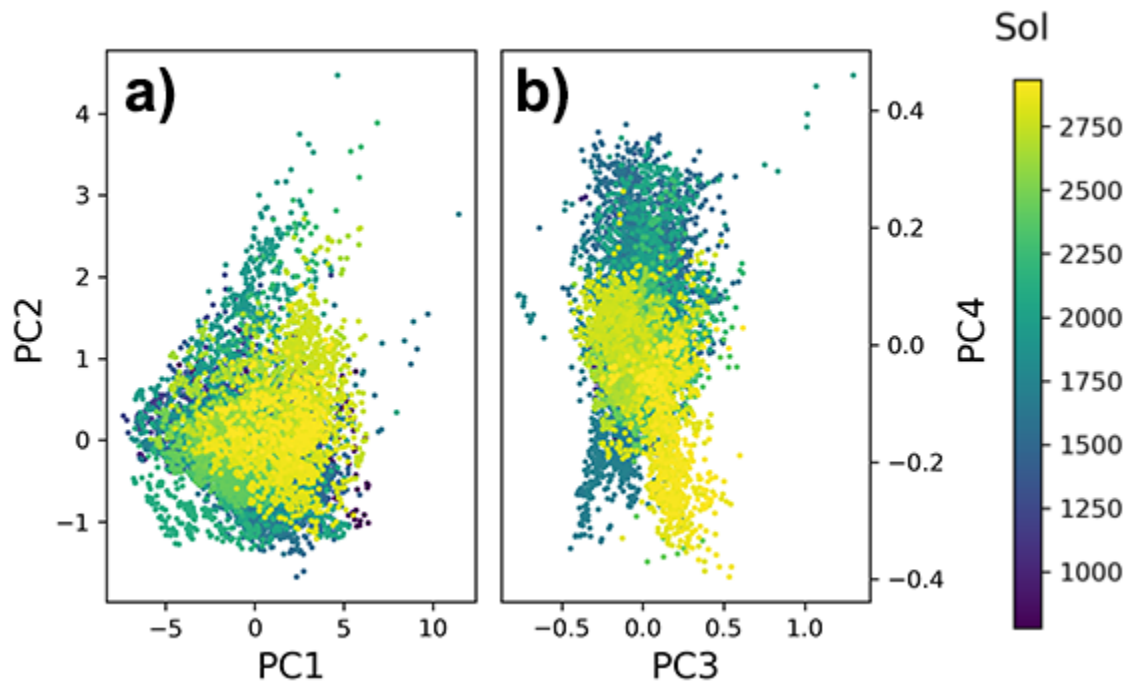
341



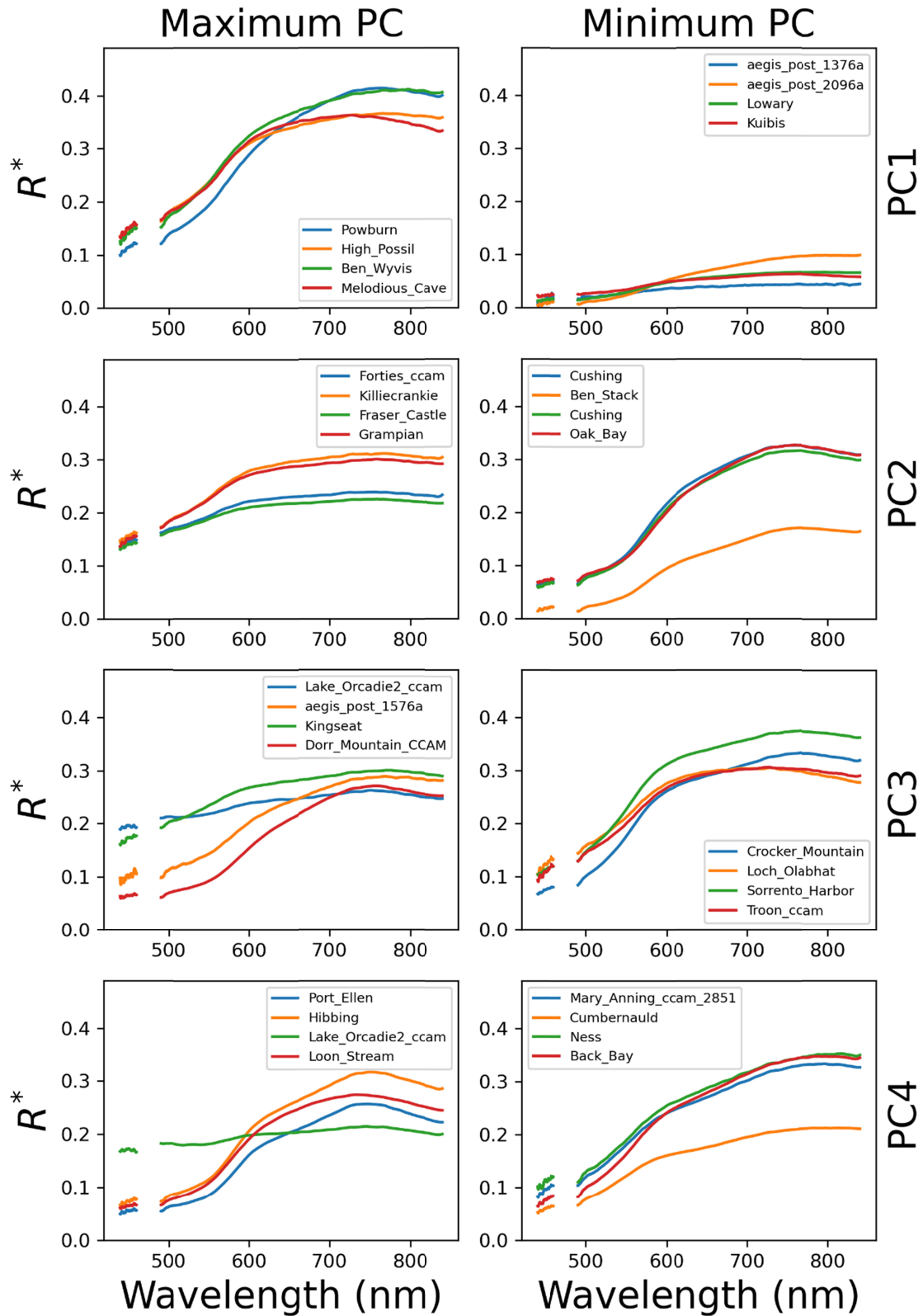
342 **Figure 3.** (a) PC1, (b) PC2, (c) PC3, and (d) PC4 plotted against spectral parameters. Negative
 343 band depth values indicate the spectrum is concave at that wavelength. Colored by sol.



344 **Figure 4.** The PC loadings plotted against wavelength for (a) PCs 1-4 and (b) PCs 5-8. The
 345 greater the loading value is above zero for a given wavelength and a given PC, the more that
 346 wavelength range positively contributes to that PC. The more negative the loading is, the more
 347 that wavelength range negatively contributes to that PC. A loading near zero indicates that region
 348 is not important for that given PC.



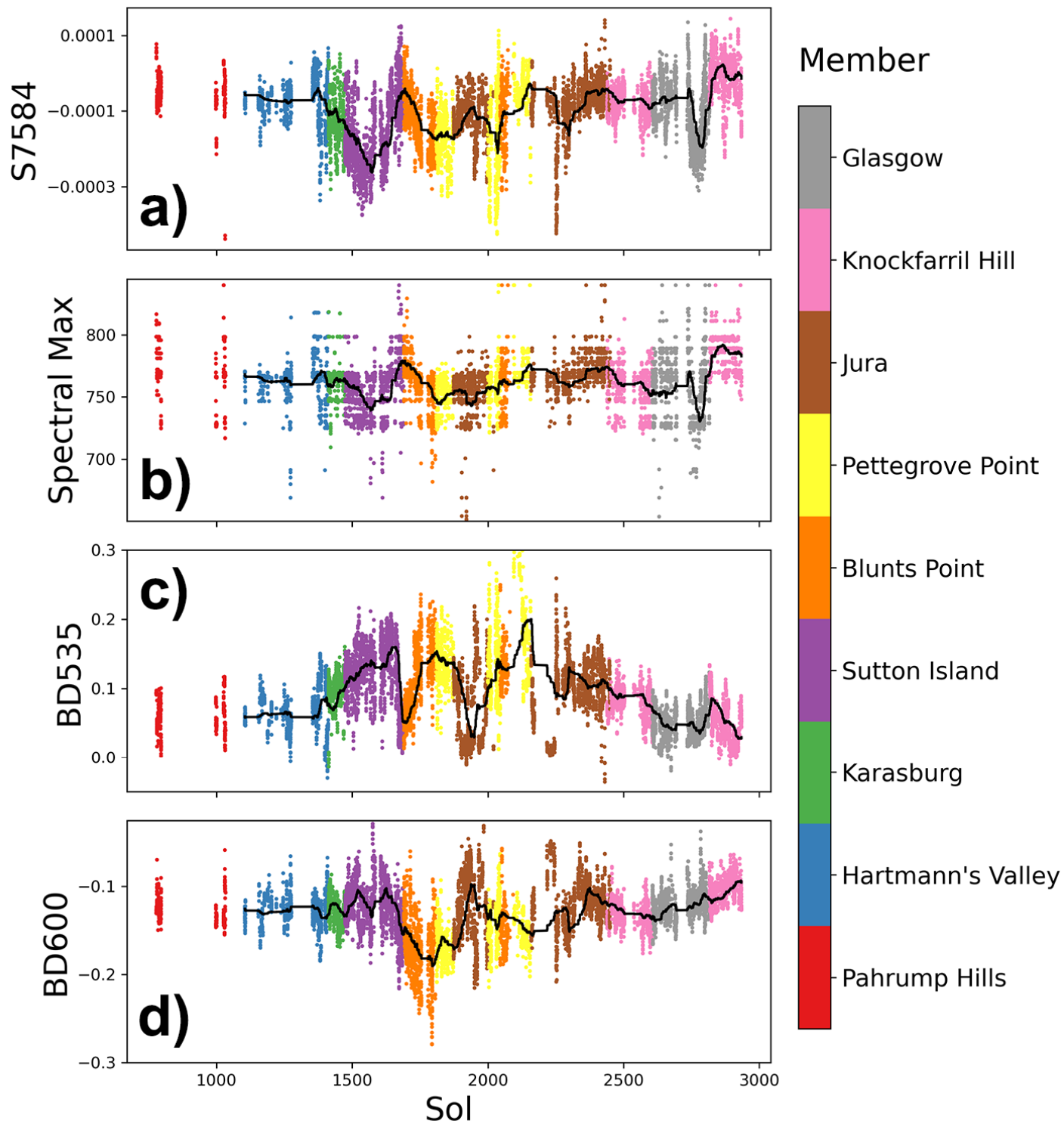
349 **Figure 5.** (a) PC2 plotted against PC1 and (b) PC4 plotted against PC3. Colored by sol number.



350 **Figure 6.** ChemCam passive spectra randomly chosen within the 150 observations with
 351 maximum (left) and minimum (right) values of PCs 1-4. Data near the VIO and NIR detector
 352 edges (460-490 nm) have low SNR and have been removed for visualization purposes.

353 4.2 Passive Spectral Parameters

354 There are variations in the calculated passive spectral parameters over Curiosity's traverse (Table
355 2), expanded here from previous work (e.g., Johnson et al., 2015, 2016; Fraeman et al., 2020).
356 BD535 increases until the boundary between Sutton Island and Blunts Point (sol 1690) where it
357 then decreases (Fig. 7c). This is mirrored by S7584, which broadly decreases until sol 1690
358 where it increases briefly (Fig. 7a), and it is also mirrored by the spectral maximum which peaks
359 around sol 1690 (Fig. 7b). Another rapid decrease in BD535 is seen in Jura, followed by a more
360 gradual decrease during the rest of the traverse. There is a small peak in BD535 near the area in
361 the Vera Rubin ridge (VRR) with the deepest BD860 absorptions seen by CRISM from orbit (sol
362 ~2004) (Fraeman et al., 2020). BD600, which is related to the strength of the short wavelength
363 ferric oxide absorption edge (Morris et al., 1985; Johnson et al., 2015), largely stays between -
364 0.05 and 0.15, except for the Jura member where it dips to as low as -0.28 (Fig. 7d). Negative
365 band depth values indicate concavity in a spectrum, not an absorption. Many of the passive
366 spectral parameters are correlated with each other (Table 3).



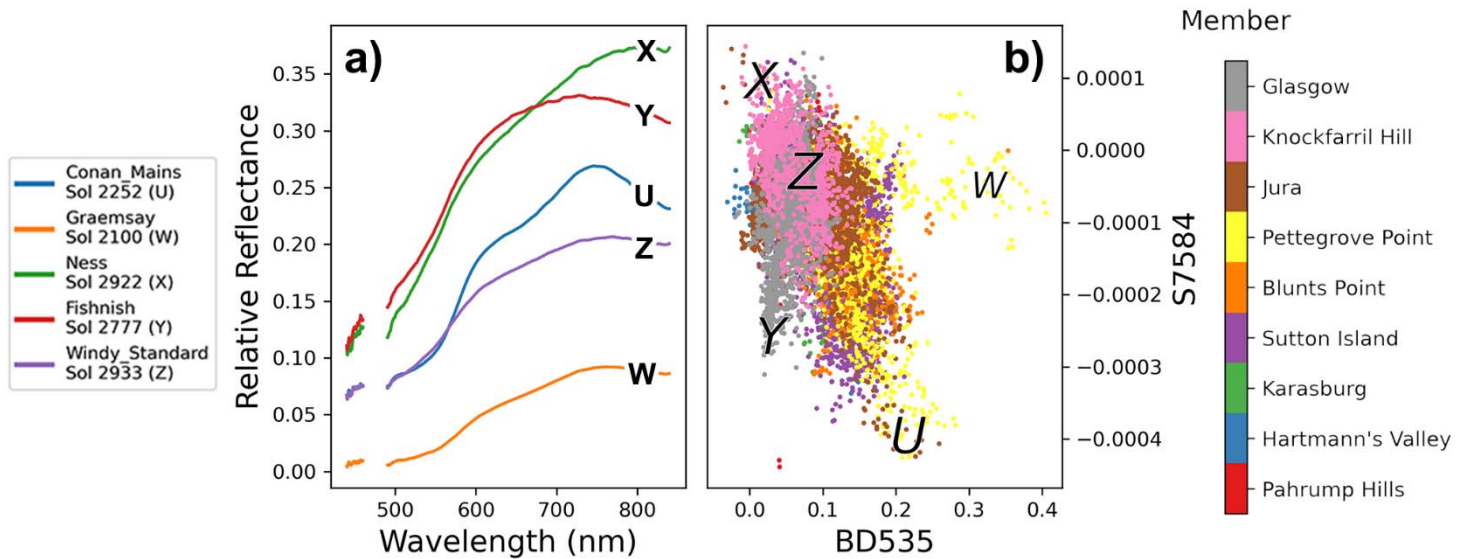
367 **Figure 7.** S7584 (a), Spectral maximum (b), BD535 (c), and BD600 (d) plotted against sol. Data
 368 are colored by geologic member. Running average of 250 observations (black line) is included.
 369
 370
 371

372 **Table 3.** A Spearman's ρ Correlation Matrix of ChemCam Passive spectra

	Sol	PC1	PC2	PC3	PC4	BD535	BD600	S7584	R6744	R6084	Spectral Maximum	Avg. Relative Reflectance
Sol	1.00	0.09	0.14	0.15	-0.26	-0.27	0.19	0.26	0.01	-0.08	0.17	0.10
PC1	0.09	1.00	-0.09	-0.04	0.01	-0.16	0.16	-0.13	0.12	-0.02	0.09	0.99
PC2	0.14	-0.09	1.00	-0.14	-0.02	-0.74	0.26	0.02	-0.91	0.81	-0.25	0.01
PC3	0.15	-0.04	-0.14	1.00	0.01	0.07	0.60	0.25	-0.09	-0.53	0.35	-0.04
PC4	-0.26	0.01	-0.02	0.01	1.00	0.50	0.00	-0.84	-0.11	0.22	-0.72	0.01
BD535	-0.27	-0.16	-0.74	0.07	0.50	1.00	-0.42	-0.40	0.62	-0.50	-0.16	-0.24
BD600	0.19	0.16	0.26	0.60	0.00	-0.42	1.00	0.16	-0.35	-0.11	0.10	0.20
S7584	0.26	-0.13	0.02	0.25	-0.84	-0.40	0.16	1.00	0.04	-0.33	0.77	-0.12
R6744	0.01	0.12	-0.91	-0.09	-0.11	0.62	-0.35	0.04	1.00	-0.69	0.25	0.03
R6084	-0.08	-0.02	0.81	-0.53	0.22	-0.50	-0.11	-0.33	-0.69	1.00	-0.54	0.06
Spectral Maximum	0.17	0.09	-0.25	0.35	-0.72	-0.16	0.10	0.77	0.25	-0.54	1.00	0.06
Avg. Relative Reflectance	0.10	0.99	0.01	-0.04	0.01	-0.24	0.20	-0.12	0.03	0.06	0.06	1.00

373

374 **4.3 Spectral Endmembers**



375 **Figure 8.** (a) Relative reflectance plotted against wavelength for five endmember spectra. (b)
 376 S7584 plotted against BD535, colored by geologic member, for all passive ChemCam
 377 observations in the dataset. Letters U-Z in (b) correspond to the spectra shown in (a), which are
 378 averages for a given target. Low SNR data around the VIO/NIR detector gap (~460-490 nm)
 379 have been removed.

380

381 Results from the above principal component analysis show focusing on trends in BD535 and
 382 S7584 is a good way to visualize spectral variability of the dataset. Plotting these two spectral

383 parameters on a scatter plot reveals five distinct classes of spectra. Combined large BD535
384 values and negative NIR slopes (S7584) are typical of ferric oxides (e.g. Fraeman et al., 2020);
385 an example of a ChemCam target with these features (“Conan Mains”, point U) is shown in Fig.
386 8. “Ness”, Point X (Fig. 8), is a target with no near-infrared (NIR) slope and near-zero BD535.
387 “Fishnish”, Point Y (Fig. 8), is a target representative of many measurements from the Glasgow
388 member that have large NIR slopes but weak to near-zero BD535. “Windy Standard” Point Z,
389 (Fig. 8), is spectrally similar to the average Murray and Carolyn Shoemaker formation bedrock,
390 with BD535 of ~0.08 and S7584 between 0 and -0.0001.

391
392 Some spectra were affected by a dust storm. “Graemsay”, Point W (Fig. 8), is a target with very
393 strong BD535, low average relative reflectance, and anomalously high R6744 and is
394 characteristic of ChemCam passive spectral observations taken during the 2018 global dust
395 storm. The dust storm significantly increased dust optical depth at 880 nm (τ) as measured by the
396 Mastcam instrument on Curiosity, reaching a maximum of $\tau=8.5$ around sol 2100 (Guzewich et
397 al., 2019). This resulted in poorly calibrated ChemCam relative reflectance observations with
398 unusually high atmospheric dust contamination, in particular low average relative reflectance,
399 very high band depth at 535 nm, and a ratio of the reflectance at 670 nm to 440 nm between 10
400 and 30. There are 44 of these dust storm points representing 15 distinct targets between sol 2093
401 and 2130.

402 403 **4.4 Passive spectra compared to LIBS data**

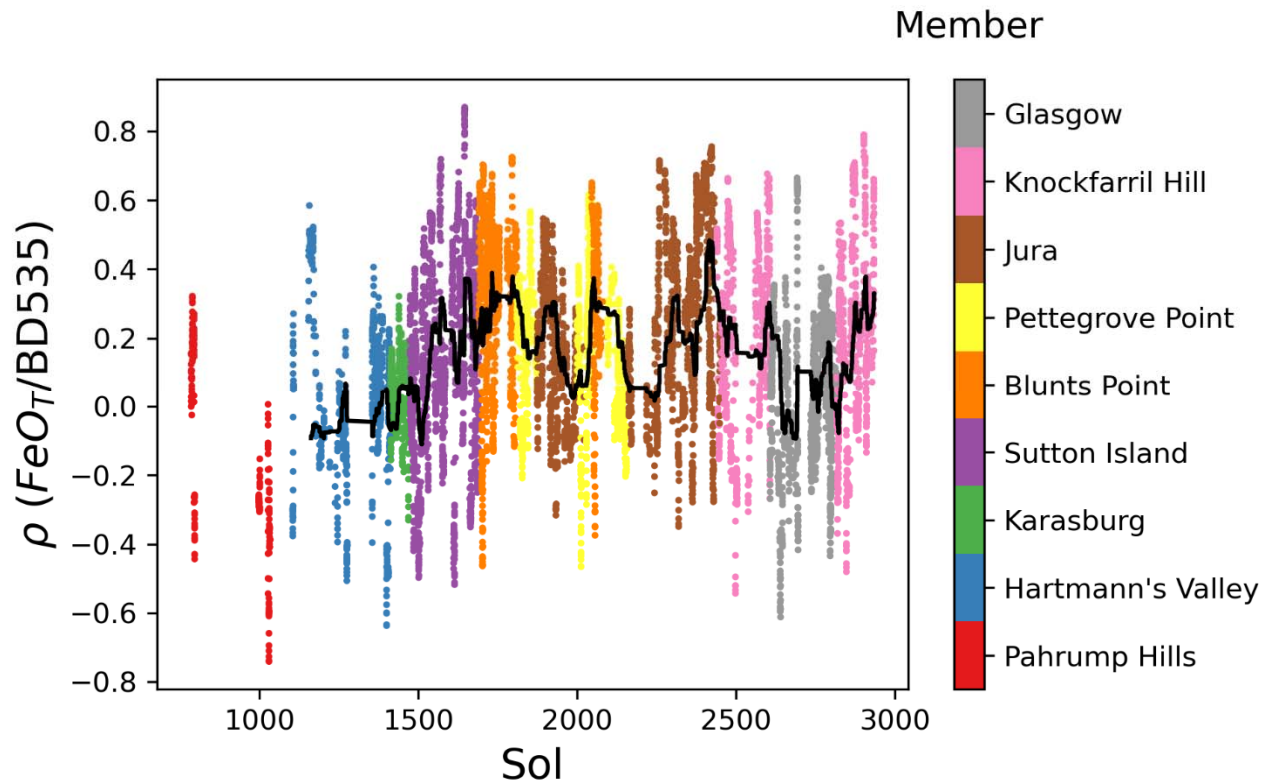
404 Correlations between passive spectral properties and elemental abundances measured by LIBS
405 were explored to search for additional insight into the sources of spectral variability and
406 compositional trends in Mt. Sharp bedrock. Of particular interest was any relationship (or lack
407 thereof) between spectral parameters and FeO_T , since the VNIR spectral range is sensitive to
408 charge-transfer and crystal-field absorptions most commonly associated with iron-bearing
409 minerals. Correlations between spectral parameters and other elements could also highlight
410 compositionally distinct regions.

411
412 When considering all Mt. Sharp group bedrock targets, no correlations between any of the major
413 or trace oxides measured by LIBS and passive spectral features were found (Table 4). Ferric
414 related spectral parameters such as PC2 and BD535 did not have any correlation with the iron
415 oxide totals (FeO_T) from LIBS observations ($\rho = -0.03$ and 0.17 respectively, Table 4) when
416 viewed over the entire traverse, there were weak correlations in a subset of rock targets near the
417 transition between the Sutton Island and Blunts Point stratigraphic members (Figure 9). There
418 were also weak correlations ($\rho \approx -0.5$) between PC4 and high magnesium targets (Fig. 10a) in the
419 Sutton Island-Blunts Point transition (~sol 1690), as well as in the Knockfarril Hill member.
420 Examination of spectra of high MgO targets in both of these regions show they have weak
421 BD535 and shallow S7584 (Point X, Fig. 8; Fig. 11). In these same two stratigraphic intervals,
422 correlations between PC4 and high MnO targets were even more apparent (Fig. 10b). Targets
423 that were examined around sol 1690 (near the Sutton Island – Blunts Point transition) have very
424 low PC4 and high weight percent MnO, whereas the surrounding rocks have both much higher
425 PC4 and low MnO values (Fig. 10b).

426
427

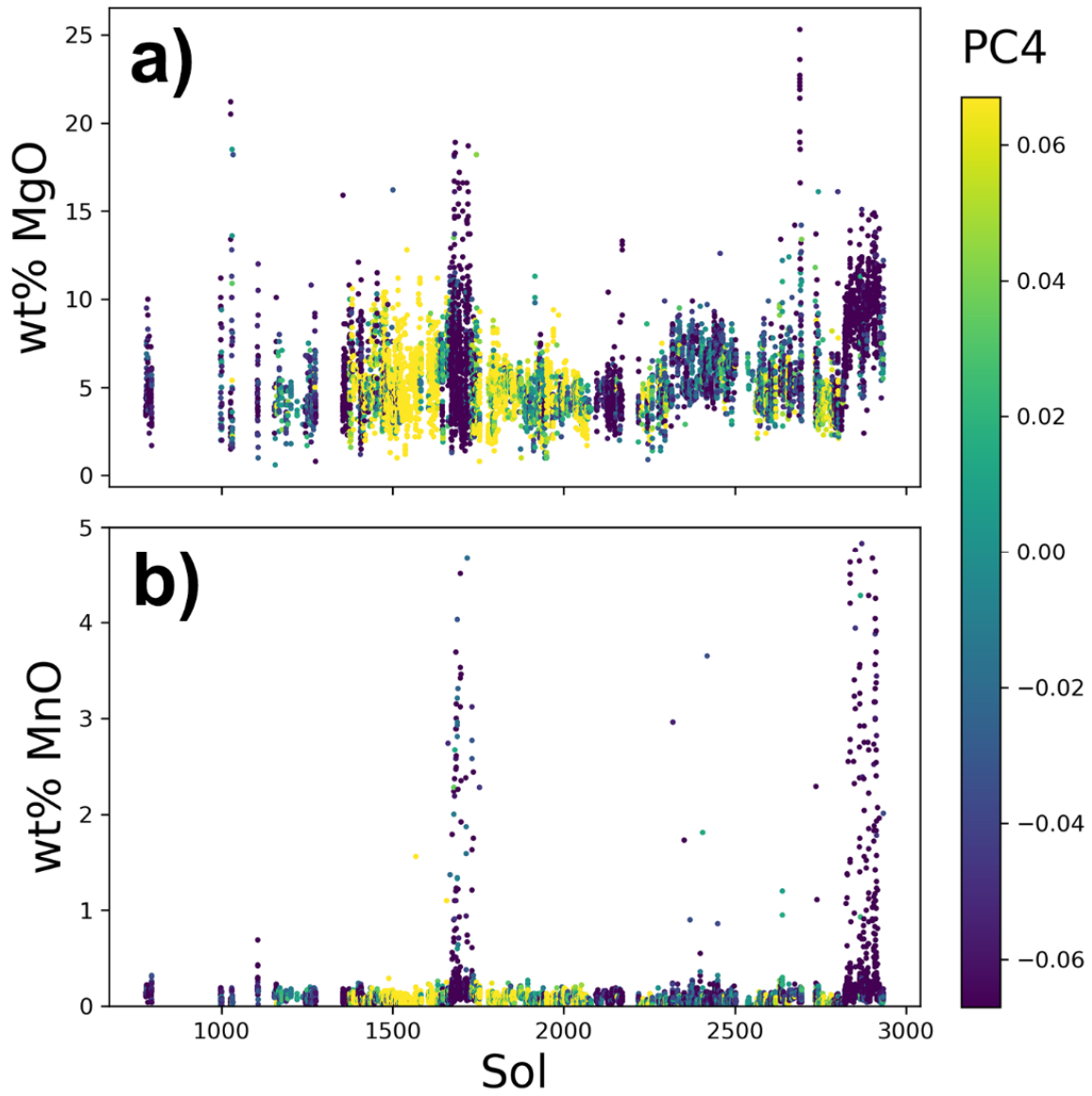
428 **Table 4.** A Spearman's ρ Correlation Matrix of ChemCam Passive and LIBS Data

	Sol	PC1	PC2	PC3	PC4	BD535	BD600	S7584	R6744	R6084	Spectral Maximum	Avg. Relative Reflectance
FeO_T	-0.12	-0.24	-0.03	-0.04	0.15	0.17	-0.14	-0.13	-0.01	0.07	-0.17	-0.24
MgO	0.17	-0.02	-0.19	0.14	-0.22	-0.04	0.14	0.20	0.17	-0.28	0.22	-0.04
SiO₂	0.23	-0.01	-0.11	0.16	0.06	0.09	0.13	0.07	0.12	-0.20	0.04	-0.02
K₂O	0.15	-0.16	-0.05	0.12	0.15	0.18	0.04	-0.04	0.03	-0.09	-0.08	-0.16
Al₂O₃	-0.02	0.07	-0.06	-0.01	0.04	0.04	0.06	0.03	0.08	-0.05	0.01	0.07
CaO	-0.17	0.14	0.24	-0.24	-0.07	-0.22	-0.12	0.00	-0.18	0.30	-0.03	0.16
Na₂O	0.00	-0.03	0.10	0.03	0.02	-0.06	0.10	0.07	-0.08	0.06	-0.03	-0.02
TiO₂	0.04	-0.08	0.04	0.07	0.14	0.03	0.08	-0.06	-0.04	0.04	-0.12	-0.07
MnO	-0.07	0.07	0.01	-0.11	-0.36	-0.18	-0.13	0.20	0.01	0.01	0.23	0.06

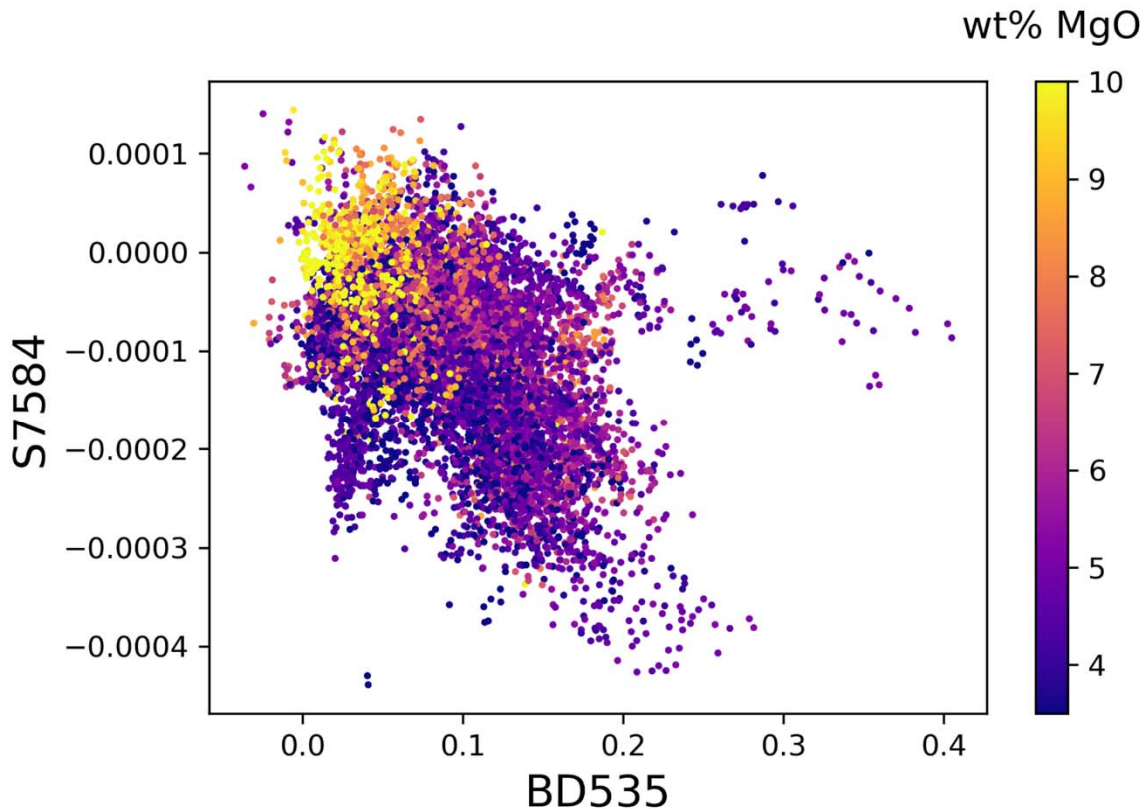


429 **Figure 9.** A rolling Spearman's correlation coefficient (ρ) of FeO_T and BD535 with a window of
 430 50 points. A rolling average of this data over 250 observations is plotted in black.

431
 432 Although not evident in the bulk measurements, there is some relationship between PC4 and
 433 high magnesium targets (Fig. 10a). This is particularly obvious around the Sutton Island-Blunts
 434 Point transition (\sim sol 1690) and in Knockfarril Hill (an example spectrum is shown as point X in
 435 Fig. 8). This appears to stem from the fact that high MgO targets have shallow BD535 and little
 436 S7584 (Fig. 11). The same is true, and even more apparent, of high MnO targets. The sols
 437 immediately around sol 1690 have very low PC4 and weight percent MnO, whereas the
 438 surroundings have much higher PC4 and MnO values (Fig. 10b).



439 **Figure 10.** Weight percent MgO and MnO plotted against sol. Colored by PC4.



440 **Figure 11.** S7584 plotted against BD535. The points are colored by weight percent MgO,
 441 showing that high MgO correlates with low BD535 and high S7584. Outlying points at the right
 442 side of the plot near S7584 ~0 are due to poor calibration during the global dust storm.
 443

444 Somewhat weaker correlations ($0.4 < \rho < 0.7$) between spectral parameters and LIBS chemistry
 445 when examined by individual stratigraphic member include:

- 446 • In Sutton Island, SiO₂ is negatively correlated with PC2 ($\rho = -0.44$) and MnO is
 447 correlated with PC4 ($\rho = -0.49$).
- 448 • In Blunts Point, all the major oxides are correlated with R6744 (and by extension PC2).
 449 R6744 is correlated with FeO_T, MgO, SiO₂, K₂O, Al₂O₃, CaO, TiO₂, and Na₂O ($\rho = 0.52,$
 450 $0.41, 0.65, 0.63, 0.59, -0.60, 0.55,$ and 0.57 respectively). BD535 is correlated with K₂O
 451 and MnO ($\rho = 0.44$ and -0.55 respectively). MnO and PC4 are also correlated ($\rho = -0.44$).
- 452 • In Knockfarril Hill, PC3 is correlated with MgO and MnO ($\rho = 0.58$ and 0.47
 453 respectively). PC4 is correlated with FeO_T, MgO, K₂O, and MnO ($\rho = 0.49, -0.70, 0.45,$
 454 and -0.65 respectively). BD535 is correlated with FeO_T, MgO, SiO₂, K₂O, and MnO ($\rho =$
 455 $0.40, -0.59, 0.45, 0.62,$ and -0.68 respectively).
- 456 • In Glasgow, S7584 is correlated with K₂O and MnO ($\rho = -0.40$ and 0.50 respectively).
 457

458 **4.5 Comparison to CheMin Data**

459 Although collected much more rarely than ChemCam LIBS data, co-located CheMin
 460 mineralogical data may provide additional insight into the source(s) of the spectral variability in
 461 the Mount Sharp group rocks. Wellington et al., (2017) found correlations between CheMin

462 analyses and Mastcam multispectral observations of drill tailings that suggested (1) the 800 nm
 463 spectral peak and 930 nm minimum in Yellowknife Bay (a Bradbury Group target) was derived
 464 from Fe-bearing phyllosilicates and pyroxenes, and (2) the 527 nm absorption in both Mastcam
 465 and ChemCam spectral data of Pahrump Hills target was consistent with the presence of
 466 crystalline hematite. Jacob et al., (2020) similarly examined CheMin data with coordinated
 467 Mastcam multispectral observations of drill tailings and hypothesized that variations in the 860
 468 nm absorption feature were the result of a combination of variations in ferric phyllosilicate
 469 abundance, variations in clinopyroxene abundance, and the presence of red crystalline hematite.

470
 471 14 targets measured by CheMin in the Murray or Carolyn Shoemaker formation over the sol
 472 range covered in this analysis have both passive and LIBS data collected before drilling (Table 5,
 473 6).

474
 475 Table 5 lists two spectral parameters from ChemCam passive data, BD535 and S7584 (Table 2),
 476 related to the presence of iron bearing minerals. 3 of these 14 targets were not brushed by the
 477 Dust Removal Tool (DRT). Even though the LIBS observations that are acquired before the
 478 passive spectra are often effective at clearing dust, the difference between DRT and non-DRT
 479 targets is still noted here due to possible differences in effectiveness of dust clearing between the
 480 two techniques. Dust can increase reflectance at longer wavelengths and can also reduce the
 481 depth of absorption features (Rice et al., 2022). Table 6 lists abundance of ferric materials
 482 inferred from CheMin data in these targets. Hematite and total ferric phase weight percent values
 483 in Table 6 are renormalized to 100% crystalline (i.e., without the amorphous components).
 484 Although there was evidence that many of the phyllosilicates in Gale crater also have some
 485 amount of Fe³⁺, they contain variable amounts of Fe²⁺ versus Fe³⁺ in the octahedral sites, so were
 486 excluded in this comparison (Tu et al., 2021).

487
 488 **Table 5.** Average BD535 and S7584 parameter values from ChemCam passive spectra for
 489 targets with both CheMin and ChemCam Data in the Murray and Carolyn Shoemaker
 490 Formations
 491

Drill Name	ChemCam Target Name	Sol	BD535	S7584 (10 ⁻⁴)
Marimba	Marimba	1418	0.107	-0.43
Quela	Quela_DRT_ccam*	1456	0.091	-0.64
Sebina	Sebina_ccam	1492	0.125	-1.95
Duluth	Duluth_ccam	2053	0.126	-0.65
Highfield	Rosebrae*	2227	0.008	-1.20
Rock Hall	Rock_Hall_ccam_1	2257	0.114	-1.62
	Rock_Hall_ccam_2	2257	0.125	-2.06
	Rock_Hall_ccam_3	2257	0.115	-2.04
	Rock_Hall_ccam_4	2259	0.107	-1.08
Aberlady	Aberlady_ccam	2367	0.089	-0.71
Kilmarie	Aberlady_ccam [†]	2367	0.089	-0.71
Glen Etive 1	Glen Etive 1_ccam	2482	0.097	-0.72
Hutton	Hutton_ccam	2666	0.020	-0.85
	Hutton2_ccam		0.043	-0.31

Glasgow	Glasgow_2_ccam* Canongate*	2753	0.071 0.040	-0.49 -1.38
Mary Anning	Mary_Anning_ccam	2831	0.054	0.73
Mary Anning 3	Mary_Anning_3_ccam	2869	0.03	0.26
Groken	Groken_ccam	2906	0.022	0.27

492 **Note.** Stoer was not included as it was in a period of high optical tau (the 2018 global dust
493 storm).

494 *Quela, Highfield, and Glasgow did not have ChemCam data from a DRT surface.

495 †Aberlady_ccam was used for both the Aberlady and Kilmorie drills as they are very close to one
496 another.

497

498 **Table 6.** CheMin data for targets in the Murray and Carolyn Shoemaker formation with both
499 CheMin and ChemCam data

500

Drill Name	Crystalline Hematite (wt%)	Total Crystalline Ferric Phases (wt%)	FeO _T in Amorphous Component (wt%)	Hematite Crystallite Size (nm)
Marimba	16.4 ± 2.1	17.9 ± 2.6	29.7	38.4
Quela	20.0 ± 1.5	21.4 ± 2.1	20.4	25.1
Sebina	20.4 ± 1.7	23.0 ± 2.3	18.8	26.8
Duluth	13.0 ± 0.8	13.0 ± 0.8	26.1	17.9
Highfield	20.2 ± 1.3	20.2 ± 1.3	7.4	30.7
Rock Hall	5.4 ± 0.4	21.0 ± 2.2	17.5	39.4
Aberlady	5.5 ± 1.4	5.5 ± 1.4	15.2	26.8
Kilmorie	3.8 ± 1.0	3.8 ± 1.0	12.4	<i>No data</i>
Glen Etive 1	7.0 ± 2.5	7.0 ± 2.5	14.4	19.7
Hutton	4.8 ± 1.2	4.8 ± 1.2	8.4	28.1
Glasgow	13.4 ± 3.1	13.4 ± 3.1	12.3	16.2
Mary Anning	2.5 ± 1.6	2.5 ± 1.6	21.4	15.6
Mary Anning 3	1.9 ± 0.5	1.9 ± 0.5	21.2	26.8
Groken	0.0	0.0	20.3	31.3

501 **Note.** Total crystalline ferric phases are CheMin-derived hematite, jarosite, and akaganeite
502 abundances added together; magnetite is not included as it does not have ferric spectral
503 expressions at 535 nm. CheMin abundances data were obtained from the Planetary Data System
504 (Vaniman, 2022). FeO_T in amorphous component is normalized to 100% amorphous. FeO_T in
505 amorphous component and hematite crystallite size were obtained from Achilles et al. (2020),
506 Rampe et al. (2020), and Thorpe et al. (2022).

507

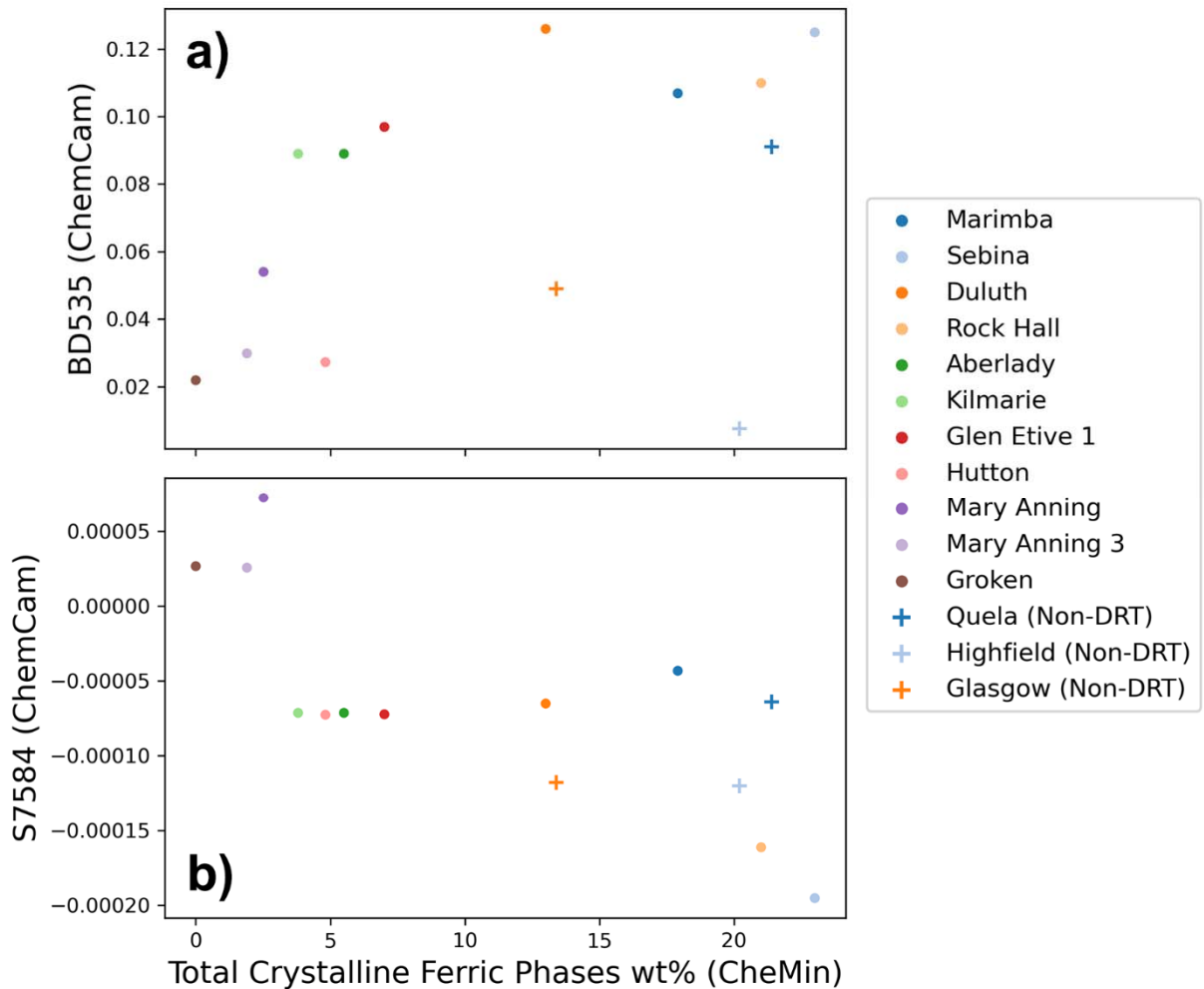
508 Highfield had a higher abundance of hematite than would be expected based on its weak 535 nm
509 absorption and lack of downturn from 750-840 nm. This was interpreted to suggest that that
510 hematite in that sample was coarse-grained “gray hematite” (Jacob et al., 2020; Rampe et al.,
511 2020b). For sufficiently large hematite particles (>~3-5 μm), the ferric absorption edge is weak
512 or not present, meaning it is approximately spectrally neutral over visible wavelengths, imparting
513 a black to gray color (Catling & Moore, 2003; Lane et al., 2002; Morris et al., 2020). When

514 Highfield is not included, there was a strong correlation ($\rho = 0.75$) between BD535 and weight
 515 percent of total crystalline ferric phases as reported by CheMin (Fig. 12a, Table 7). This is
 516 consistent with findings from Mastcam multispectral data (Jacob et al., 2020; Rice et al., 2022;
 517 Wellington et al., 2017). S7584 was correlated with crystalline ferric phases ($\rho = -0.61$, Fig.
 518 12b) and with weight percent amorphous FeO_T ($\rho = 0.66$). The target with the highest average
 519 BD535 and steepest NIR slope (Sebina_ccam) corresponded to the sample with the most total
 520 crystalline ferric phases measured by CheMin (23 wt%). The target with the lowest weight
 521 percent ferric phases (Groken) was also the ChemCam target with the lowest average BD535 and
 522 very little S7584. Importantly, there were no targets with ChemCam-observed absorptions
 523 attributed to ferric iron that were not found to contain ferric phases as measured by CheMin. This
 524 indicates that the total abundance of crystalline ferric phases was a major source of variation in
 525 ChemCam passive reflectance spectra, with weight percent amorphous FeO_T also playing a role.
 526 As demonstrated by Highfield, grain size of the ferric phases can also affect passive reflectance
 527 spectra.

529 **Table 7.** A Spearman's ρ Correlation Matrix of ChemCam Passive and Co-located CheMin
 530 Mineralogy Data

	BD535	S7584	Hematite	Ferric Phases	Amorphous FeO_T	Hematite size
BD535	1	-0.37	0.68	0.75	0.34	-0.03
S7584	-0.37	1	-0.48	-0.61	0.66	-0.14
Hematite	0.68	-0.48	1	0.92	0.08	-0.16
Ferric Phases	0.75	-0.61	0.92	1	0.04	0.07
Amorphous FeO_T	0.34	0.66	0.08	0.04	1	-0.03
Hematite size	-0.03	-0.14	-0.16	0.07	-0.03	1

531 **Note.** Highfield was not included in this analysis.



532 **Figure 12.** (a) BD535 and (b) S7584 derived from ChemCam passive observations vs. total
 533 crystalline ferric phases (hematite, jarosite, and akaganeite) from CheMin for all Mt. Sharp group
 534 drill holes for which a corresponding ChemCam observation. Targets marked with a cross
 535 represent observations not taken on a DRT surface.

536

537 **5 Discussion**

538 **5.1 Summary of Spectral Variability in ChemCam Passive Spectra**

539 PCA demonstrates that, after average relative reflectance, the biggest driver of variability in
 540 ChemCam passive spectra of Mt. Sharp group rocks are changes in ferric-related spectral
 541 absorptions. PC2 explains 6.61% of the variance of the dataset, and it is correlated with the depth
 542 of the 535 nm absorption (Fe^{3+} electronic pair transition) (Fig. 3b), visible slope or “redness”
 543 (R6744), and near infrared slope (R6084). PC3, with 0.42% of the variance, is loosely correlated
 544 with BD600, which is related to the strength of the ferric oxide absorption edge (Fig. 3c), and
 545 PC4 (0.22% of the variance) is correlated with the slope from 750 nm and 840 nm, which is also
 546 related to electron transitions in ferric minerals (Fig. 3d). Loading plots for PCs 5-8 show a large
 547 increase in noise below 500 nm (Fig. 4b), and PCs 5-8 were not found to meaningfully relate to
 548 any spectral parameters.

549

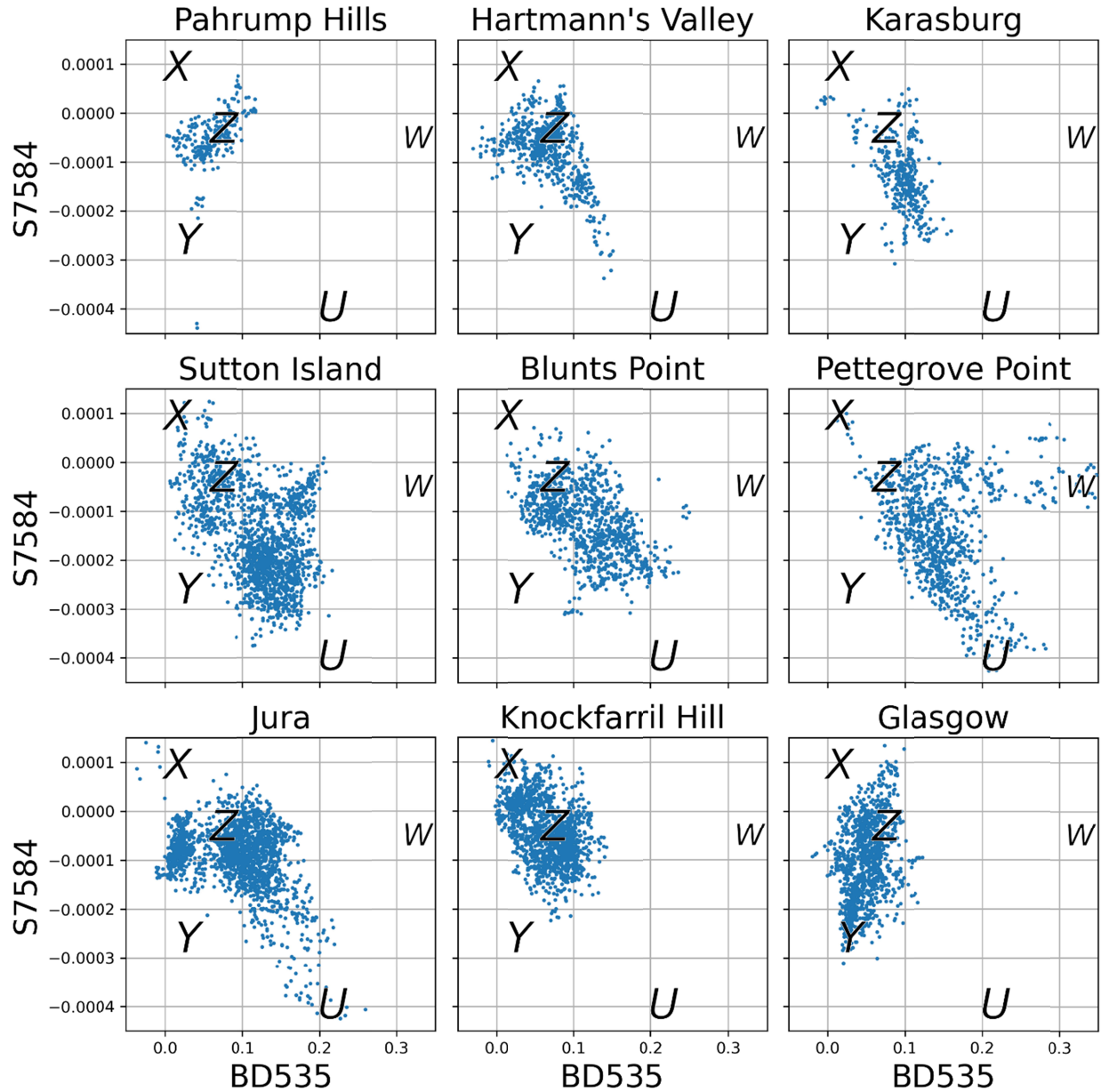
550 Calculated passive spectral parameters varied significantly across the rover traverse. BD535
551 broadly increased until Pettegrove Point, near the VRR, where it decreased towards Glasgow and
552 Knockfarril Hill. There was also a significant decrease in BD535 near sol 1690 which was
553 mirrored by an increase in the NIR slope and the spectral maximum approaching 840 nm (see
554 Section 5.3). A small peak in BD535 occurred near the area in the VRR with the strongest
555 BD860 absorptions seen by CRISM from orbit (sol ~2004), although it was only moderately
556 higher than other parts of the traverse (Fraeman et al., 2020).

557
558 The depth of the 535 nm absorption (~PC2) and S7584 (~PC4) cannot be used as a direct proxy
559 for amount of iron oxides or ferric materials in a sample; factors such as mineral grain sizes and
560 mineral mixtures also have also been shown to affect the strength of these features in Mt. Sharp
561 group rocks (Jacob et al., 2020; Wellington et al. 2017). However, the 14 samples of Murray and
562 Carolyn Shoemaker formation bedrock analyzed by CheMin that had corresponding ChemCam
563 passive observations did show a correlation between strength of these absorption features and
564 total ferric phases in the sample (Fig. 12), demonstrating abundance of ferric phases is an
565 important driver in the presence and depth of these absorptions. The target with the highest
566 abundance of ferric phases as measured by CheMin, Sebina, had a deep 535 nm absorption and
567 strong NIR slope, while the target with the lowest abundance of ferric phases, Groken, had very
568 little BD535 and flat NIR slopes (Fig. 12).

569
570 These findings are consistent with complementary Curiosity datasets. Spectral variations in
571 Mastcam multispectral data are dominated by spectral differences that are attributed to hematite
572 and other oxides (Rice et al., 2022; Jacob et al., 2020). Rice et al., (2022) identified nine distinct
573 classes of Mastcam rock spectra from sols 0-2302, some of which are broadly similar to the
574 ChemCam passive spectral endmembers identified in this work. For example, Class “U” (Fig. 8
575 and Fig. 13) is analogous to Class 4 (Hexriver) from Rice et al., (2022), both being consistent
576 with red fine-grained hematite. Although a fewer number of samples were analyzed, CheMin
577 analyses of drilled samples from the Murray formation varied in the amount and types of
578 oxidized phases they contain (Bristow et al., 2018; Rampe et al., 2020a).

579 580 **5.2 Spectrally unique areas**

581 Figure 13 plots S7584 vs BD535 (correlated with PC4 and PC2 respectively), which reveals
582 trends and spectrally unique regions in Mt. Sharp. Rocks in the Pettegrove Point member and
583 portions of the Jura member associated with Vera Rubin ridge, have the highest combined
584 BD535 and S7584 (class “U” in Fig. 8 and Fig. 13), as well as the lowest BD535 and S7584
585 (class “X”). The unique spectral properties in this area have been explored in detail (Fraeman et
586 al., 2020; Horgan et al., 2020; Jacob et al., 2020; L’Haridon et al., 2020) and a leading
587 hypothesis is hematite of variable grain sizes formed by diagenesis, possibly in association with
588 the destruction of clay minerals by silica-poor brines (Bristow et al., 2021). Two other groups of
589 spectrally distinct ChemCam passive observations include those taken in the Glasgow member
590 and during the 2018 global dust storm. Each of these are discussed below.



591 **Figure 13.** S7584 plotted against BD535 in each geologic member of the Mt. Sharp group.
 592 Spectral classes “U” through “Z” from Fig. 8 are also plotted for context.

593

594 5.2.1 Glasgow Member and the Hutton Interval

595 The transition between the Knockfarril Hill and Glasgow members is spectrally unique. Most
 596 Knockfarril Hill member targets have spectral features similar to average Mt. Sharp group
 597 bedrock (small BD535 and S7584 values), whereas many Glasgow targets have low BD535 and
 598 strongly negative NIR slopes (point Y in Fig. 8 and 13). The spectral difference could be the
 599 result of average Murray/Carolyn Shoemaker bedrock mixing with a new spectral endmember
 600 with less abundance or coarser grained ferric phases. Interestingly, analyses of sedimentary
 601 structures in this area showed a change in lithology that marked a significant transition from
 602 dominantly lacustrine to fluvial environments (Caravaca et al., 2022; Fedo et al., 2022). The
 603 concurrent changes in lithology and spectral properties could therefore be indicative of

604 compositional variations that either reflect that shift in primary depositional environment and/or
605 different styles of diagenesis in this area.

606

607 A shift towards stronger S7584 but still shallow BD535 occurs around sol 2750-2800, at an area
608 referred to as the Hutton interval. This interval occurs in the Glasgow member below the Siccar
609 Point unconformity, and it is also associated with a color change in Mastcam color images, as
610 well as a unique chemistry and mineralogy (Dehouck et al., 2022; Rudolph et al., 2022;
611 Thompson et al., 2022; Thorpe et al., 2022). Specifically, the Hutton interval in the Glasgow
612 member is characterized by a decrease in chemical index of alteration (CIA) values, localized
613 enrichments and depletions in mobile elements, and significant amount of cristobalite and opal-
614 CT (Dehouck et al., 2022; O’Connell-Cooper et al., 2022; Thorpe et al., 2022).

615

616 There are two endmember hypotheses to explain the unique composition of the Hutton interval:
617 (1) there was a significant shift in the alteration conditions and/or nature of sediment source or
618 (2) this interval is a region of enhanced diagenesis related to the Siccar Point unconformity (e.g.
619 Dehouck et al., 2022). Each scenario predicts a different regional distribution of Hutton interval
620 type material with respect to the Siccar Point unconformity, which Curiosity will have a chance
621 to test to if it re-visits the unconformity at a higher elevation. If the Hutton interval is related to
622 the diagenesis along the unconformity, rocks with similar compositional characteristics will re-
623 appear. If the interval is related to depositional environments, the rocks near the Siccar Point
624 unconformity to the south may be different. The discovery that the Hutton interval unconformity
625 has unique spectral properties will provide additional criteria to test these hypotheses from
626 Curiosity remote sensing data (whose acquisition is less resource intensive than drill sample
627 collection for CheMin).

628

629 **5.2.2 Targets acquired during high tau**

630 ChemCam observations taken during the 2018 global dust storm were readily identified by their
631 passive spectral features (class “W” in Fig. 8), in particular average relative reflectance below
632 0.085, BD535 above 0.3, and R6744 between 10 and 30. R6744 (the red-blue ratio) has been
633 used as a first order approximation for dust cover at the Mars Pathfinder landing site (Johnson et
634 al., 2003) and is similarly useful in ChemCam passive spectra. R6744 values above 10 occur
635 exclusively during the 2018 dust storm between sol 2093 and 2130. We include dust storm
636 observations here (44 measurements of 15 distinct targets) for completeness but note that
637 spectral parameter correlations for these observations should be considered separately. This is
638 evidenced by their very high BD535 but weak S7584 values (e.g., Fig 11), which are consistent
639 with shadowed targets (Johnson et al., 2015).

640

641 **5.3 Comparison between spectral and chemical properties of bedrock targets**

642 Active LIBS chemical data collected from the same locations as passive spectral data provide a
643 unique opportunity to directly compare chemical and spectral properties of Mt. Sharp bedrock.

644

645 Weight percent FeO_T reported by LIBS and BD535 from passive spectra are not correlated
646 (Spearman’s $\rho = 0.18$) on the scale of Curiosity’s traverse or generally within any individual
647 member. The decoupled nature of FeO_T and BD535 demonstrates that regions with strong 535
648 nm absorptions bands, like the Vera Rubin ridge, are not associated with areas where iron was
649 added to the host bedrock (David et al., 2020), for example by being carried by anoxic

650 groundwater and subsequently precipitating at a redox interface (as proposed by Fraeman et al.,
651 2013).

652
653 Interestingly, there was an increase in the correlation strength between FeO_T and BD535 near the
654 boundary of Sutton Island and Blunts Point and a small increase in Knockfarril Hill (Fig. 9) –
655 two areas that are notable for their relatively high weight percent MnO targets (Fig. 10b). The
656 presence of MnO is an indication of strongly oxidizing conditions (Lanza et al., 2016), but across
657 the traverse there is no monotonic relationship between this potential signature of iron oxidation
658 (the correlation coefficient of FeO_T and BD535) and weight percent MnO.

659
660 The comparison of passive relative reflectance spectra and LIBS elemental data highlighted the
661 boundary of Sutton Island and Blunts Point (sol 1690) as an area of interest. This region was
662 proposed to be an interval of low lake level, as indicated by the presence of highly soluble
663 hydrated magnesium sulfates associated with the bedrock detected both in-situ (Rapin et al.,
664 2019) and from orbit (Sheppard et al., 2021). These magnesium sulfate rich bedrock targets were
665 found to have significantly lower PC4 than the surrounding terrain (Fig. 10), corresponding to
666 near zero S7584 (Fig. 7a), weak BD535 (Fig. 7c), and a spectral maximum approaching 800 nm
667 (Fig 7b). This is consistent with Mastcam observations which suggest a significant decrease in
668 crystalline hematite relative to the rest of the Murray formation and an increase in other iron
669 bearing phases with band centers past the wavelength range of ChemCam (~910-930 nm) such as
670 Fe/Mg smectite, jarosite, and akaganeite (Haber et al., 2022). This compositional change is
671 indicative of more surface exposure and a low stand environment as described in Rapin et al.,
672 2019. In clearly identifying this important region, principal component analysis of passive
673 spectra has demonstrated that it is a valuable tool for gaining additional geochemical insight
674 from ChemCam data.

675
676 In Blunts Point, PC2 and R6744 were moderately correlated with all major oxides reported by
677 LIBS (R6744 had positive correlations with FeO_T , MgO, SiO_2 , K_2O , Al_2O_3 , Na_2O , and TiO_2 and
678 negative correlations with CaO); (Section 4.4). This was not seen in any other stratigraphic
679 member in this dataset and is likely the result of Ca sulfate cements that were previously
680 identified in this region by ChemCam (Nellessen et al., 2019). Abundances of 10-25 wt% CaO
681 consistent across a given target is characteristic of these cements (M. Nellessen et al., 2018).
682 This is in contrast to vein observations (Fig. 2) showing pure Ca sulfates (e.g., lacking any
683 silicate component and displaying higher Ca and S signatures). These cements are likely formed
684 by Ca sulfate precipitation into the pore space prior to lithification of the sandstone. The cements
685 thus indicate a change in depositional environment, such as a change in deposition rate, or more
686 likely, a shoreline environment in which evaporation-dominated areas are separated from the
687 main body of the lake (e.g., Rapin et al. 2019).

688 689 **6 Conclusions**

690 Passive relative reflectance spectra of bedrock targets taken by ChemCam in the Murray and
691 Carolyn Shoemaker formations were analyzed using principal component analysis (PCA),
692 spectral parameters, and compared to their corresponding LIBS elemental abundances. PCA of
693 ChemCam passive spectra proved useful in highlighting geochemically distinct regions of the
694 traverse. The Blunts Point-Sutton Island transition, which contains magnesium sulfate rich
695 targets and has been proposed as an area of low lake level by Rapin et al. (2019), was found to

696 have zero 750 nm to 840 nm spectral slope (PC4) and weak 535 nm band depth (PC2), in
697 agreement with Mastcam data from this interval (Haber et al., 2022). The Hutton interval (sol
698 2750-2800) was found to be spectrally distinct from the rest of the Mt. Sharp group, having
699 strong 750 nm to 840 nm spectral slope slopes but little change in 535 nm band depth. This
700 indicates either a change in alteration conditions or enhanced diagenesis in this region.
701 Comparisons between spectral parameters and LIBS data in Blunts point also suggest influences
702 from calcium cements. The correlation coefficient between FeO_T reported by LIBS and BD535
703 from passive spectra was investigated as a tool for understanding changing oxidation conditions
704 across Curiosity's traverse. Higher than average correlations between FeO_T and BD535 were
705 found in the Blunts Point-Sutton Island transition and Knockfarril Hill, regions known to be rich
706 in MnO, but this signature of oxidizing conditions was not found to rise to significance on the
707 scale of the traverse.

708

709 **Acknowledgements**

710 A portion of this research was carried out at the Jet Propulsion Laboratory, California Institute of
711 Technology, under a contract with the National Aeronautics and Space Administration
712 (80NM0018D0004). This work was funded by the JPL SURF Program, the NASA MSL
713 Participating Scientist Program, and NASA's Mars Exploration Program support to the Mars
714 Science Laboratory Mission. JF acknowledges the support from the Carlsberg Foundation. OG
715 work on the ChemCam instrument supported by CNES.

716

717 **Data Availability Statement**

718 The MSL ChemCam Passive Surface Spectra bundle (Johnson, 2022) was obtained from the
719 Planetary Data System (PDS). CheMin and LIBS data were also obtained from the PDS
720 (Vaniman, 2022; Wiens, 2022). MSL Localizations for mapping were acquired on the PDS
721 (Deen, 2015).

722

723 **References**

724 Achilles, C. N., Rampe, E. B., Downs, R. T., Bristow, T. F., Ming, D. W., Morris, R. V., et al.

725 (2020). Evidence for Multiple Diagenetic Episodes in Ancient Fluvial-Lacustrine

726 Sedimentary Rocks in Gale Crater, Mars. *Journal of Geophysical Research: Planets*,

727 *125*(8). <https://doi.org/10.1029/2019JE006295>

728 Anderson, R. B., Morris, R. V., Clegg, S. M., Bell, J. F., Wiens, R. C., Humphries, S. D., et al.

729 (2011). The influence of multivariate analysis methods and target grain size on the

730 accuracy of remote quantitative chemical analysis of rocks using laser induced

731 breakdown spectroscopy. *Icarus*, *215*(2), 608–627.

732 <https://doi.org/10.1016/j.icarus.2011.07.034>

733

734 Anderson, R. C., Jandura, L., Okon, A. B., Sunshine, D., Roumeliotis, C., Beegle, L. W., et al.
735 (2012). Collecting Samples in Gale Crater, Mars; an Overview of the Mars Science
736 Laboratory Sample Acquisition, Sample Processing and Handling System. *Space Science*
737 *Reviews*, 170(1–4), 57–75. <https://doi.org/10.1007/s11214-012-9898-9>

738 Bell, J. F. III McCord, T. B., & Owensby, P. D. (1990). Observational evidence of crystalline
739 iron oxides on Mars. *Journal of Geophysical Research*, 95(B9), 14447.
740 <https://doi.org/10.1029/JB095iB09p14447>

741 Bell, J. F. III McSween, H. Y., Crisp, J. A., Morris, R. V., Murchie, S. L., Bridges, N. T., et al.
742 (2000). Mineralogic and compositional properties of Martian soil and dust: Results from
743 Mars Pathfinder. *Journal of Geophysical Research: Planets*, 105(E1), 1721–1755.
744 <https://doi.org/10.1029/1999JE001060>

745 Bell, J. F. III, Godber, A., McNair, S., Caplinger, M. A., Maki, J. N., Lemmon, M. T., et al.
746 (2017). The Mars Science Laboratory *Curiosity* rover Mastcam instruments: Preflight and
747 in-flight calibration, validation, and data archiving. *Earth and Space Science*, 4(7), 396–
748 452. <https://doi.org/10.1002/2016EA000219>

749 Bennett, K. A., Fox, V. K., Bryk, A., Dietrich, W., Fedo, C., Edgar, L., et al. (2022). The
750 *Curiosity* Rover’s Exploration of Glen Torridon, Gale crater, Mars: An Overview of the
751 Campaign and Scientific Results. *Journal of Geophysical Research: Planets*.
752 <https://doi.org/10.1029/2022JE007185>

753 Blake, D., Vaniman, D., Achilles, C., Anderson, R., Bish, D., Bristow, T., et al. (2012).
754 Characterization and Calibration of the CheMin Mineralogical Instrument on Mars
755 Science Laboratory. *Space Science Reviews*, 170(1–4), 341–399.
756 <https://doi.org/10.1007/s11214-012-9905-1>

757 Bristow, T. F., Grotzinger, J. P., Rampe, E. B., Cuadros, J., Chipera, S. J., Downs, G. W., et al.
758 (2021). Brine-driven destruction of clay minerals in Gale crater, Mars. *Science*,
759 373(6551), 198–204. <https://doi.org/10.1126/science.abg5449>

760 Bristow, T. F., Rampe, E. B., Achilles, C. N., Blake, D. F., Chipera, S. J., Craig, P., et al. (2018).
761 Clay mineral diversity and abundance in sedimentary rocks of Gale crater, Mars. *Science*
762 *Advances*, 4(6), eaar3330. <https://doi.org/10.1126/sciadv.aar3330>

763 Calef III, F. J., & Parker, T. (2016). MSL Gale Merged Orthophoto Mosaic. PDS Annex, U.S.
764 Geological Survey. Retrieved from http://bit.ly/MSL_Basemap

765 Caravaca, G., Mangold, N., Dehouck, E., Schieber, J., Zaugg, L., Bryk, A. B., et al. (2022). From
766 Lake to River: Documenting an Environmental Transition across the Jura/Knockfarril
767 Hill Members Boundary in the Glen Torridon Region of Gale crater (Mars). *Journal of*
768 *Geophysical Research: Planets*. <https://doi.org/10.1029/2021JE007093>

769 Catling, D. C., and Moore, J. M. (2003). The nature of coarse-grained crystalline hematite and its
770 implications for the early environment of Mars. *Icarus*, 165(2), 277–300.
771 [https://doi.org/10.1016/S0019-1035\(03\)00173-8](https://doi.org/10.1016/S0019-1035(03)00173-8)

772 Clegg, S. M., Wiens, R. C., Anderson, R., Forni, O., Frydenvang, J., Lasue, J., et al. (2017).
773 Recalibration of the Mars Science Laboratory ChemCam instrument with an expanded
774 geochemical database. *Spectrochimica Acta Part B: Atomic Spectroscopy*, 129, 64–85.
775 <https://doi.org/10.1016/j.sab.2016.12.003>

776 David, G., Cousin, A., Forni, O., Meslin, P. -Y., Dehouck, E., Mangold, N., et al. (2020).
777 Analyses of High-Iron Sedimentary Bedrock and Diagenetic Features Observed With
778 ChemCam at Vera Rubin Ridge, Gale Crater, Mars: Calibration and Characterization.

779 *Journal of Geophysical Research: Planets*, 125(10).
780 <https://doi.org/10.1029/2019JE006314>

781 Deen, R. (2015). MSL Mars Rover 6 RDR PLACES Rover Motion Counter V1.0 [Data set].
782 NASA Planetary Data System. <https://doi.org/10.17189/1520397>

783 Dehouck, E., Cousin, A., Mangold, N., Frydenvang, J., Gasnault, O., Forni, O., et al. (2022).
784 Bedrock geochemistry and alteration history of the clay-bearing Glen Torridon region of
785 Gale crater, Mars. *Journal of Geophysical Research: Planets*.
786 <https://doi.org/10.1029/2021JE007103>

787 Edgar, L. A., Fedo, C. M., Gupta, S., Banham, S. G., Fraeman, A. A., Grotzinger, J. P., et al.
788 (2020). A Lacustrine Paleoenvironment Recorded at Vera Rubin Ridge, Gale Crater:
789 Overview of the Sedimentology and Stratigraphy Observed by the Mars Science
790 Laboratory Curiosity Rover. *Journal of Geophysical Research: Planets*, 125(3).
791 <https://doi.org/10.1029/2019JE006307>

792 Farrand, W. H., Bell, J. F., Johnson, J. R., Rice, M. S., & Hurowitz, J. A. (2013). VNIR
793 multispectral observations of rocks at Cape York, Endeavour crater, Mars by the
794 Opportunity rover's Pancam. *Icarus*, 225(1), 709–725.
795 <https://doi.org/10.1016/j.icarus.2013.04.014>

796 Fedo, C. M., Bryk, A. B., Edgar, L. A., Bennett, K. A., Fox, V. K., Dietrich, W. E., et al. (2022).
797 Geology and Stratigraphic Correlation of the Murray and Carolyn Shoemaker Formations
798 Across the Glen Torridon Region, Gale Crater, Mars. *Journal of Geophysical Research:*
799 *Planets*, 127(9). <https://doi.org/10.1029/2022JE007408>

800 Fraeman, A. A., Arvidson, R. E., Catalano, J. G., Grotzinger, J. P., Morris, R. V., Murchie, S. L.,
801 et al. (2013). A hematite-bearing layer in Gale Crater, Mars: Mapping and implications

802 for past aqueous conditions. *Geology*, 41(10), 1103–1106.
803 <https://doi.org/10.1130/G34613.1>

804 Fraeman, A. A., Johnson, J. R., Arvidson, R. E., Rice, M. S., Wellington, D. F., Morris, R. V., et
805 al. (2020). Synergistic Ground and Orbital Observations of Iron Oxides on Mt. Sharp and
806 Vera Rubin Ridge. *Journal of Geophysical Research: Planets*, 125(9).
807 <https://doi.org/10.1029/2019JE006294>

808 Gasda, P. J., Anderson, R. B., Cousin, A., Forni, O., Clegg, S. M., Ollila, A., et al. (2021).
809 Quantification of manganese for ChemCam Mars and laboratory spectra using a
810 multivariate model. *Spectrochimica Acta Part B: Atomic Spectroscopy*, 181, 106223.
811 <https://doi.org/10.1016/j.sab.2021.106223>

812 Graff, T. G., Morris, R. V., Clegg, S. M., Wiens, R. C., & Anderson, R. B. (2011). Dust Removal
813 on Mars using Laser-Induced Breakdown Spectroscopy, 1916. Presented at the 42nd
814 Annual Lunar and Planetary Science Conference.

815 Guzewich, S. D., Lemmon, M., Smith, C. L., Martínez, G., de Vicente-Retortillo, Á., Newman,
816 C. E., et al. (2019). Mars Science Laboratory Observations of the 2018/Mars Year 34
817 Global Dust Storm. *Geophysical Research Letters*, 46(1), 71–79.
818 <https://doi.org/10.1029/2018GL080839>

819 Gwizd, S., Fedo, C., Grotzinger, J., Banham, S., Rivera-Hernández, F., Stack, K. M., et al.
820 (2022). Sedimentological and Geochemical Perspectives on a Marginal Lake
821 Environment Recorded in the Hartmann’s Valley and Karasburg Members of the Murray
822 Formation, Gale Crater, Mars. *Journal of Geophysical Research: Planets*, 127(8).
823 <https://doi.org/10.1029/2022JE007280>

824 Haber, J. T., Horgan, B., Fraeman, A. A., Johnson, J. R., Bell, J. F., Rice, M. S., et al. (2022).
825 Mineralogy of a possible ancient lakeshore in the Sutton Island member of Mt. Sharp,
826 Gale crater, Mars, from Mastcam multispectral images. *Journal of Geophysical*
827 *Research: Planets*. <https://doi.org/10.1029/2022JE007357>

828 Horgan, B. H. N., Johnson, J. R., Fraeman, A. A., Rice, M. S., Seeger, C., Bell, J. F., et al.
829 (2020). Diagenesis of Vera Rubin Ridge, Gale Crater, Mars, From Mastcam
830 Multispectral Images. *Journal of Geophysical Research: Planets*, *125*(11).
831 <https://doi.org/10.1029/2019JE006322>

832 Izawa, M. R. M., Cloutis, E. A., Rhind, T., Mertzman, S. A., Applin, D. M., Stromberg, J. M.,
833 and Sherman, D. M. (2019). Spectral reflectance properties of magnetites: Implications
834 for remote sensing. *Icarus*, *319*, 525–539. <https://doi.org/10.1016/j.icarus.2018.10.002>

835 Jacob, S. R., Wellington, D. F., Bell, J. F., Achilles, C., Fraeman, A. A., Horgan, B., et al.
836 (2020). Spectral, Compositional, and Physical Properties of the Upper Murray Formation
837 and Vera Rubin Ridge, Gale Crater, Mars. *Journal of Geophysical Research: Planets*,
838 *125*(11). <https://doi.org/10.1029/2019JE006290>

839 Johnson, J. R. (2022). MSL ChemCam Passive Surface Spectra Bundle.
840 <https://doi.org/10.17189/1520577>

841 Johnson, J. R., Grundy, W. M., & Lemmon, M. T. (2003). Dust deposition at the Mars Pathfinder
842 landing site: observations and modeling of visible/near-infrared spectra. *Icarus*, *163*(2),
843 330–346. [https://doi.org/10.1016/S0019-1035\(03\)00084-8](https://doi.org/10.1016/S0019-1035(03)00084-8)

844 Johnson, J. R., Bell, J. F., Bender, S., Blaney, D., Cloutis, E., DeFlores, L., et al. (2015).
845 ChemCam passive reflectance spectroscopy of surface materials at the Curiosity landing
846 site, Mars. *Icarus*, *249*, 74–92. <https://doi.org/10.1016/j.icarus.2014.02.028>

847 Johnson, J. R., Bell, J. F., Bender, S., Blaney, D., Cloutis, E., Ehlmann, B., et al. (2016).
848 Constraints on iron sulfate and iron oxide mineralogy from ChemCam visible/near-
849 infrared reflectance spectroscopy of Mt. Sharp basal units, Gale Crater, Mars. *American*
850 *Mineralogist*, *101*(7), 1501–1514. <https://doi.org/10.2138/am-2016-5553>

851 Lane, M. D., Morris, R. V., Mertzman, S. A., & Christensen, P. R. (2002). Evidence for platy
852 hematite grains in Sinus Meridiani, Mars: PLATY HEMATITE GRAINS IN SINUS
853 MERIDIANI, MARS. *Journal of Geophysical Research: Planets*, *107*(E12), 9-1-9–15.
854 <https://doi.org/10.1029/2001JE001832>

855 Lanza, N. L., Clegg, S. M., Wiens, R. C., McInroy, R. E., Newsom, H. E., & Deans, M. D.
856 (2012). Examining natural rock varnish and weathering rinds with laser-induced
857 breakdown spectroscopy for application to ChemCam on Mars. *Appl. Opt.*, *51*(7), B74–
858 B82. <https://doi.org/10.1364/AO.51.000B74>

859 Lanza, N. L., Wiens, R. C., Arvidson, R. E., Clark, B. C., Fischer, W. W., Gellert, R., et al.
860 (2016). Oxidation of manganese in an ancient aquifer, Kimberley formation, Gale crater,
861 Mars: Manganese Fracture Fills in Gale Crater. *Geophysical Research Letters*, *43*(14),
862 7398–7407. <https://doi.org/10.1002/2016GL069109>

863 L’Haridon, J., Mangold, N., Fraeman, A. A., Johnson, J. R., Cousin, A., Rapin, W., et al. (2020).
864 Iron Mobility During Diagenesis at Vera Rubin Ridge, Gale Crater, Mars. *Journal of*
865 *Geophysical Research: Planets*, *125*(11). <https://doi.org/10.1029/2019JE006299>

866 Malin, M. C., Ravine, M. A., Caplinger, M. A., Tony Ghaemi, F., Schaffner, J. A., Maki, J. N., et
867 al. (2017). The Mars Science Laboratory (MSL) Mast cameras and Descent imager:
868 Investigation and instrument descriptions. *Earth and Space Science*, *4*(8), 506–539.
869 <https://doi.org/10.1002/2016EA000252>

870 Maurice, S., Wiens, R. C., Saccoccio, M., Barraclough, B., Gasnault, O., Forni, O., et al. (2012).
871 The ChemCam Instrument Suite on the Mars Science Laboratory (MSL) Rover: Science
872 Objectives and Mast Unit Description. *Space Science Reviews*, 170(1–4), 95–166.
873 <https://doi.org/10.1007/s11214-012-9912-2>

874 Morris, R. V., Rampe, E. B., Vaniman, D. T., Christoffersen, R., Yen, A. S., Morrison, S. M., et
875 al. (2020). Hydrothermal Precipitation of Sanidine (Adularia) Having Full Al,Si
876 Structural Disorder and Specular Hematite at Maunakea Volcano (Hawai'i) and at Gale
877 Crater (Mars). *Journal of Geophysical Research: Planets*, 125(9).
878 <https://doi.org/10.1029/2019JE006324>

879 Morris, R. V., Lauer, H. V., Lawson, C. A., Gibson, E. K., Nace, G. A., & Stewart, C. (1985).
880 Spectral and other physicochemical properties of submicron powders of hematite (α -Fe₂
881 O₃), maghemite (γ -Fe₂O₃), magnetite (Fe₃O₄), goethite (α -FeOOH), and
882 lepidocrocite (γ -FeOOH). *Journal of Geophysical Research*, 90(B4), 3126.
883 <https://doi.org/10.1029/JB090iB04p03126>

884 Nellessen, M., Baker, A. M., Newsom, H. E., Jackson, R., Williams, J., Clegg, S. M., et al.
885 (2018). Distribution and Analysis of Calcium Sulfate Cemented Sandstones Along the
886 Msl Traverse, Gale Crater, Mars, 2018, P31F-3760. Presented at the AGU Fall Meeting
887 Abstracts.

888 Nellessen, M. A., Baker, A. M., Newsom, H. E., Jackson, R. S., Williams, J., Nachon, M., et al.
889 (2019). Distribution and Analysis of Calcium Sulfate-Cemented Sandstones Along the
890 MSL Traverse, Gale Crater, Mars, 3031. Presented at the 50th Annual Lunar and
891 Planetary Science Conference.

892 O'Connell-Cooper, C. D., Thompson, L. M., Spray, J. G., Berger, J. A., Gellert, R., McCraig,
893 M., et al. (2022). Statistical Analysis of APXS-Derived Chemistry of the Clay-Bearing
894 Glen Torridon Region and Mount Sharp Group, Gale Crater, Mars. *Journal of*
895 *Geophysical Research: Planets*, 127(9). <https://doi.org/10.1029/2021JE007177>

896 Pearson, K. (1901). LIII. *On lines and planes of closest fit to systems of points in space. The*
897 *London, Edinburgh, and Dublin Philosophical Magazine and Journal of Science*, 2(11),
898 559–572. <https://doi.org/10.1080/14786440109462720>

899 Pedregosa, F., Varoquaux, G., Gramfort, A., Michel, V., Thirion, B., Grisel, O., et al. (2012).
900 Scikit-learn: Machine Learning in Python (Version 4).
901 <https://doi.org/10.48550/ARXIV.1201.0490>

902 Pelkey, S., and Jakosky, B. (2002). Surficial Geologic Surveys of Gale Crater and Melas
903 Chasma, Mars: Integration of Remote-Sensing Data. *Icarus*, 160(2), 228–257.
904 <https://doi.org/10.1006/icar.2002.6978>

905 Peret, L., Gasnault, O., Dingler, R., Langevin, Y., Bender, S., Blaney, D., et al. (2016).
906 Restoration of the Autofocus capability of the ChemCam instrument onboard the
907 Curiosity rover. In *SpaceOps 2016 Conference*. Daejeon, Korea: American Institute of
908 Aeronautics and Astronautics. <https://doi.org/10.2514/6.2016-2539>

909 Rampe, E. B., Blake, D. F., Bristow, T. F., Ming, D. W., Vaniman, D. T., Morris, R. V., et al.
910 (2020). Mineralogy and geochemistry of sedimentary rocks and eolian sediments in Gale
911 crater, Mars: A review after six Earth years of exploration with Curiosity. *Geochemistry*,
912 80(2), 125605. <https://doi.org/10.1016/j.chemer.2020.125605>

913 Rampe, E. B., Bristow, T. F., Morris, R. V., Morrison, S. M., Achilles, C. N., Ming, D. W., et al.
914 (2020). Mineralogy of Vera Rubin Ridge From the Mars Science Laboratory CheMin

915 Instrument. *Journal of Geophysical Research: Planets*, 125(9).
916 <https://doi.org/10.1029/2019JE006306>

917 Rapin, W., Ehlmann, B. L., Dromart, G., Schieber, J., Thomas, N. H., Fischer, W. W., et al.
918 (2019). An interval of high salinity in ancient Gale crater lake on Mars. *Nature*
919 *Geoscience*, 12(11), 889–895. <https://doi.org/10.1038/s41561-019-0458-8>

920 Rice, M. S., Seeger, C., Bell, J., Calef, F., St. Clair, M., Eng, A., et al. (2022). Spectral Diversity
921 of Rocks and Soils in Mastcam Observations Along the Curiosity Rover’s Traverse in
922 Gale Crater, Mars. *Journal of Geophysical Research: Planets*, 127(8).
923 <https://doi.org/10.1029/2021JE007134>

924 Rudolph, A., Horgan, B., Johnson, J., Bennett, K., Haber, J., Bell, J. F., et al. (2022). The
925 distribution of clay minerals and their impact on diagenesis in Glen Torridon, Gale crater,
926 Mars. *Journal of Geophysical Research: Planets*. <https://doi.org/10.1029/2021JE007098>

927 Savitzky, A., & Golay, M. J. E. (1964). Smoothing and Differentiation of Data by Simplified
928 Least Squares Procedures. *Analytical Chemistry*, 36(8), 1627–1639.
929 <https://doi.org/10.1021/ac60214a047>

930 Sheppard, R. Y., Milliken, R. E., Parente, M., & Itoh, Y. (2021). Updated Perspectives and
931 Hypotheses on the Mineralogy of Lower Mt. Sharp, Mars, as Seen From Orbit. *Journal of*
932 *Geophysical Research: Planets*, 126(2). <https://doi.org/10.1029/2020JE006372>

933 Sherman, D. M. (1985). The electronic structures of Fe³⁺ coordination sites in iron oxides:
934 Applications to spectra, bonding, and magnetism. *Physics and Chemistry of Minerals*,
935 12(3), 161–175. <https://doi.org/10.1007/BF00308210>

936 Sherman, D. M. and Waite, T. D. (1985). Electronic spectra of Fe³⁺ oxides and oxide
937 hydroxides in the near IR and near UV. *American Mineralogist*, 70, 1262–1269.

938 Sherman, D. M., Burns, R. G., & Burns, V. M. (1982). Spectral characteristics of the iron oxides
939 with application to the Martian bright region mineralogy. *Journal of Geophysical*
940 *Research*, 87(B12), 10169. <https://doi.org/10.1029/JB087iB12p10169>

941 Spearman, C. (1904). The Proof and Measurement of Association between Two Things. *The*
942 *American Journal of Psychology*, 15(1), 72. <https://doi.org/10.2307/1412159>

943 Stack, K. M., Cofield, S. M., Fraeman, A. A., & Edwards, C. S. (2016). Geologic Map of the
944 MSL Curiosity Rover Extended Mission Traverse of Aeolis Mons, Gale Crater, Mars (p.
945 283395). Presented at the GSA Annual Meeting in Denver, Colorado, USA - 2016.
946 <https://doi.org/10.1130/abs/2016AM-283395>

947 Stack, K. M., Grotzinger, J. P., Lamb, M. P., Gupta, S., Rubin, D. M., Kah, L. C., et al. (2019).
948 Evidence for plunging river plume deposits in the Pahrump Hills member of the Murray
949 formation, Gale crater, Mars. *Sedimentology*, 66(5), 1768–1802.
950 <https://doi.org/10.1111/sed.12558>

951 Thompson, L. M., Spray, J. G., O’Connell-Cooper, C., Berger, J. A., Yen, A., Gellert, R., et al.
952 (2022). Alteration at the Base of the Siccar Point Unconformity and Further Evidence for
953 an Alkaline Provenance at Gale Crater: Exploration of the Mount Sharp Group,
954 Greenheugh Pediment Cap Rock Contact With APXS. *Journal of Geophysical Research:*
955 *Planets*, 127(11). <https://doi.org/10.1029/2021JE007178>

956 Thomson, B. J., Bridges, N. T., Milliken, R., Baldrige, A., Hook, S. J., Crowley, J. K., et al.
957 (2011). Constraints on the origin and evolution of the layered mound in Gale Crater,
958 Mars using Mars Reconnaissance Orbiter data. *Icarus*, 214(2), 413–432.
959 <https://doi.org/10.1016/j.icarus.2011.05.002>

960 Thorpe, M. T., Bristow, T. F., Rampe, E. B., Tosca, N. J., Grotzinger, J. P., Bennett, K. A., et al.
961 (2022). Mars Science Laboratory CheMin data from the Glen Torridon region and the
962 significance of lake-groundwater interactions in interpreting mineralogy and sedimentary
963 history. *Journal of Geophysical Research: Planets*.
964 <https://doi.org/10.1029/2021JE007099>

965 Tu, V. M., Rampe, E. B., Bristow, T. F., Thorpe, M. T., Clark, J. V., Castle, N., et al. (2021). A
966 Review of the Phyllosilicates in Gale Crater as Detected by the CheMin Instrument on
967 the Mars Science Laboratory, Curiosity Rover. *Minerals*, 11(8), 847.
968 <https://doi.org/10.3390/min11080847>

969 Vaniman, D. (2022). MSL Mars Chemistry and Mineralogy 4 RDR V1.0 [Data set]. NASA
970 Planetary Data System. <https://doi.org/10.17189/1519497>

971 Vasavada, A. R. (2022). Mission Overview and Scientific Contributions from the Mars Science
972 Laboratory Curiosity Rover After Eight Years of Surface Operations. *Space Science*
973 *Reviews*, 218(3), 14. <https://doi.org/10.1007/s11214-022-00882-7>

974 Viviano, C. E., Seelos, F. P., Murchie, S. L., Kahn, E. G., Seelos, K. D., Taylor, H. W., et al.
975 (2014). Revised CRISM spectral parameters and summary products based on the
976 currently detected mineral diversity on Mars. *Journal of Geophysical Research: Planets*,
977 119(6), 1403–1431. <https://doi.org/10.1002/2014JE004627>

978 Wellington, D. F., Bell, J. F., Johnson, J. R., Kinch, K. M., Rice, M. S., Godber, A., et al. (2017).
979 Visible to near-infrared MSL/Mastcam multispectral imaging: Initial results from select
980 high-interest science targets within Gale Crater, Mars. *American Mineralogist*, 102(6),
981 1202–1217. <https://doi.org/10.2138/am-2017-5760CCBY>

982 Wiens, R.C. (2022). MSL Mars ChemCam LIBS Spectra 4/5 RDR V1.0 [Data set]. NASA
983 Planetary Data System. <https://doi.org/10.17189/1519485>
984 Wiens, R. C., Maurice, S., Barraclough, B., Saccoccio, M., Barkley, W. C., Bell, J. F., et al.
985 (2012). The ChemCam Instrument Suite on the Mars Science Laboratory (MSL) Rover:
986 Body Unit and Combined System Tests. *Space Science Reviews*, 170(1–4), 167–227.
987 <https://doi.org/10.1007/s11214-012-9902-4>
988